Repeatability of land-based controlled-source electromagnetic measurements in industrialized areas and including vertical electric fields

Kristina Tietze,[1,*] Oliver Ritter,[1,2] Cedric Patzer,[1,2] Paul Veeken[3,†] and Meindert Dillen[3]

[1]*GFZ German Research Centre for Geosciences, Telegrafenberg, D-14473 Potsdam, Germany. E-mail: ktietze@gfz-potsdam.de*
[2]*Department of Earth Sciences, Freie Universität, Malteserstr. 74–100, D-12249 Berlin, Germany*
[3]*Wintershall Dea GmbH, Friedrich-Ebert-Str. 160, D-34119 Kassel, Germany*

ABSTRACT

Over the last decade, an increasing number of numerical studies have proposed controlled-source electromagnetic (CSEM) techniques for monitoring of fluid flow in reservoirs, for example, in the framework of hydrocarbon production or CO_2 storage scenarios. A fundamental prerequisite for any monitoring application in practice is repeatability of the measurements, particularly in areas with high noise levels.

Here, we report on CSEM data acquired across a producing oil field on land in three consecutive surveys between 2014 and 2016. As major conductivity changes in the reservoir structure are not expected for this time frame, the data sets provide an excellent basis to study accuracy and repeatability of such measurements over a time span of 2.5 yr.

Our results show that uncertainties of single CSEM measurements lie between 0.1 and 10 per cent with a focus around 1 per cent in all surveys. For source–receiver offsets <2 km uncertainties are in the range of ∼0.1–0.3 per cent, proportional to the transfer function amplitudes, and are dominated by intrinsic noise of the measuring system. At source–receiver distances >4 km external noise resulting from natural electromagnetic field variations and powered installations dominates uncertainties that assume minimum absolute values of 10^{-9}–$10^{-10}\,\mathrm{V\,A^{-1}\,m^{-1}}$ with lowest values at frequencies between 0.1 and 10 Hz.

Overall, repeatability of CSEM measurements depends on a range of factors, including source–receiver distances, component of the transfer function, source-polarization and relocation errors, in particular at sites close to the source, where the geometry and characteristics of the source fields vary rapidly in space. Best repeatability was observed for receiver stations at 2–4 km distance from the source and frequencies <20 Hz. At these stations, phases and amplitudes of transfer functions usually agreed within $\pm1°$ and ±5 per cent between measurements. Such values are in a range as expected from time-lapse signals due to resistivity changes in target (reservoir) formations. Hence, precise surveying procedures are essential.

We also measured the vertical electric field (E_z) with a newly developed receiver chain in a 200 m deep observation borehole. The vertical electric field component shows generally higher sensitivity to resistivity changes in reservoir structures than the horizontal electric fields measured at surface. Although amplitudes of E_z are about one to two orders of magnitude smaller than amplitudes of horizontal electric fields, recordings of E_z are stable. More importantly, E_z transfer functions of three measurements between 2015 and 2016 show excellent quality and repeatability within $<\pm2°$ and $<\pm5$ per cent, similar as horizontal electric fields indicating that noise conditions at depth improve when compared with sensors at surface.

Key words: Electrical properties; Controlled source electromagnetics (CSEM); Time-series analysis.

---

* Now at: The University of Adelaide, Adelaide, Australia.
† Now at: Geops, 22bis Rue Colonel Fabien, F-92116 Antony, France.

1 INTRODUCTION

1.1 Controlled-source electromagnetic monitoring

In recent years, an increasing number of studies have investigated the applicability of surface-based controlled-source electromagnetic (CSEM) methods for monitoring of fluid flow in the subsurface by means of imaging the distribution of electrical conductivity in the underground. In porous formations, conductivity of rocks is usually dominated by the pore fill, that is, fluids (e.g. Guéguen & Palciauskas 1994).

Most of the investigations focus on monitoring of hydrocarbon reservoirs (e.g. Wirianto *et al.* 2010; Schamper *et al.* 2011; Schaller *et al.* 2014; Strack 2014; Tietze *et al.* 2015, 2018). A comprehensive review of CSEM methods for exploration and monitoring of hydrocarbon reservoirs is provided by Streich (2016). But targets under investigation also include CO_2 storage applications (Streich *et al.* 2010; Vilamajó *et al.* 2013; Zhdanov *et al.* 2013; Börner *et al.* 2015b) or geothermal reservoirs (Börner *et al.* 2015a). Nearly all of the published work concludes that monitoring of the investigated subsurface process is feasible with CSEM techniques, though a few authors point out that the expected time-lapse responses are probably close to the detectability threshold (Tietze *et al.* 2015; see also Streich 2016).

Essential prerequisites for monitoring are sufficient accuracy and repeatability of measurements as well as sensitivity to the conductivity changes in the target formation. Changes of electromagnetic (EM) fields between measurements resulting from changes within the target structure have to be larger than data uncertainties. Repeatability of EM data is, therefore, determined by two major factors: (i) the accuracy or quality of individual measurements and (ii) the accuracy of replicating observations over time with continuous or time-lapse measurements.

Major constituent of the uncertainty of individual measurements taken at a particular point in time is the EM noise level. EM noise on CSEM measurements includes cultural noise emitted from technical installations, natural EM signals, noise introduced by sensors and recording equipment and inaccuracies of source and receiver set-up. EM noise levels can vary between measurements, for example, as additional infrastructure may be installed or removed in between measurements and levels of natural EM signals vary, for example, with geomagnetic activity levels. For electric field measurements on land typical observed noise floors range between 10^{-10} and 10^{-8} V m^{-1} (Girard *et al.* 2011; Vilamajó *et al.* 2013; Tietze *et al.* 2015) in operating CO_2 storage sites or oil fields.

Replication errors of time-lapse measurements should be reduced to a minimum but are in practice impossible to avoid. Such errors include relocation errors of sensors and CSEM sources (if not installed permanently), or changes in instrument responses due to alteration processes or temperature variations. A second type of errors encompasses changes of subsurface resistivities outside the target area. In particular, variations in water saturation and temperature may change resistivities in the near-surface environment.

While such potential disturbances of EM measurements and repeatability may seem obvious, there is only little empirical information on repeatability of land-based EM data published. Wirianto *et al.* (2010) provide some theoretical considerations on the various sources of repeatability errors, yet in lack of observations they finally assume that their influence on amplitudes of electric fields reaches 1 per cent at maximum. Similar values were adopted by Schamper *et al.* (2011) and Vilamajó *et al.* (2013). Tietze *et al.* (2015) presented a first repeatability test acquiring CSEM data set

in a producing oilfield 10 d apart, while part of their equipment was left in place between the two measurements. Overall, they achieved repeatability errors of 1–5 per cent for most of the data set.

For marine applications, the number of CSEM studies is much larger and a few more repeatability trials have been published (Zach *et al.* 2009; Ziolkowski *et al.* 2010; Holten & Flekkøy 2011; Myer *et al.* 2012). Myer *et al.* (2012) report differences of 3–6 per cent for CSEM measurements across the Scarborough gas field repeated after a few days without receiver relocation and 2–7 per cent if receivers were redeployed. Ziolkowski *et al.* (2010) achieved data agreement within a normalized RMS of 3.9 per cent for measurements about 1 yr apart. Major challenges for repeatability of marine data include source navigation, water currents and waves, and changes of electrical conductivity of water due to variations in salinity and temperature. As these differ from challenges on land, results from marine studies cannot be taken as reference for land measurements in general.

Here, we focus on and limit the discussion to land-based CSEM measurements. In particular, we will expand on the work of Tietze *et al.* (2015) and present CSEM time-lapse data from a producing oil field onshore Northern Germany that were acquired in three consecutive surveys over 2.5 yr between 2014 and 2016.

1.2 Measurements of the vertical electric field on land

Several modelling studies concluded that measurement of the vertical electric field (E_z) would be beneficial for monitoring of fluids in oil reservoirs on land. Numerical simulations of Wirianto *et al.* (2010), Schaller *et al.* (2014) and Tietze *et al.* (2015) suggested that sensitivity of the vertical electric field component to resistivity changes in reservoir structures is significantly higher than for horizontal electric fields measured at surface.

The results also showed that while vertical electric fields can in principle assume the same field strength as horizontal fields they often are one or more orders of magnitude smaller than horizontal components, particularly for typical field surveys using electric dipole sources at surface. In general, the vertical electric field is close to zero directly at the Earth's surface because of the extreme conductivity contrast between electrically conductive subsurface and insulating (nearly perfectly resistive) air. Also, CSEM fields excited by horizontal dipoles, residing in a 1-D horizontally layered or homogeneous structure do not contain a vertical component at source depth.

To achieve reasonable signal-to-noise levels for recordings of electric field components, usually dipole lengths of several tens of metres are required. For the vertical component, such measurements can only be realized in dedicated boreholes on land and involve significant technical and financial efforts. These efforts are probably the main reason for the scarcity of measurements of vertical electric fields. E_z data have been recorded as part of marine CSEM (e.g. Chave & Filloux 1985; Bindoff *et al.* 1986; Holten *et al.* 2009; Håland *et al.* 2012), cross-well EM and a few land-based magnetotelluric (MT) measurements (e.g. Jones & Geldart 1967a,b; Bahr 1983). So far, we have not become aware of published measurements of the vertical electric field in the framework of CSEM measurements performed on land. In particular, information on signal-to-noise ratios and repeatability of land measurements is basically non-existent.

Cross-well EM measurements use EM sources and receivers located each within a (vertical) well that is typically steel-cased (e.g.

Alumbaugh & Morrison 1995; Wilt *et al.* 1995; Colombo & Mc-Neice 2017). These casings lead to a significant distortion and attenuation of EM fields and their consideration is an essential part of the interpretation techniques of cross-well surveys. Hence, recordings and noise characteristics of electric fields of cross-well EM surveys differ substantially from measurement of vertical electric fields in uncased wells as suggested by studies of Wirianto *et al.* (2010) and Tietze *et al.* (2015). Similarly, measurements of E_z in marine CSEM surveys, where vertical electric dipoles are simply suspended in the water column of the ocean, are subject to different challenges as outlined previously in the discussion on repeatability of CSEM data.

A few studies were carried out, however, on natural variations of E_z. Electrical currents in horizontal direction are excited by MT sources outside the solid earth (Cagniard 1953). Where electrical conductivities vary laterally, that is, for 2-D and 3-D underground scenarios, currents are deflected and vertical components of electrical currents and associated fields arise. Maybe the first measurements of the vertical electric field within the solid earth ever were conducted in the 1930s in a 46 m deep uncased well in Peru (Forbush 1933). The recordings showed that natural variations occur not only for horizontal electric fields but similarly for the vertical component and signals could be correlated with changes in the horizontal magnetic fields recorded at surface. Further investigations of horizontal electric fields measured at surface and vertical electric fields within (presumably uncased) diamond drillholes in Canada by Jones & Geldart (1967a,b) showed that vertical and horizontal components at the same location are comparable in amplitude variations and spectral content for frequencies of 0.0012–0.12 Hz; similar observations were made by Bahr (1983) for E_z measurements at 1 m depth.

Lateral variations of conductivity are ubiquitous and natural variations of the vertical electric field can be expected to be present in nearly any E_z recording on land. In consideration of the results described above, noise levels of E_z for EM measurements at frequencies <0.1 Hz can be expected to be of similar level as for horizontal fields. At higher frequencies, data quality of CSEM measurements is mainly determined by the amount of cultural noise of man-made electrical installations such as powerlines, railways and other infrastructure. So far, it is unclear how such cultural noise affects E_z measurements. Yet, attenuation of EM signals in the subsurface increases with frequency. Hence, amplitudes of EM signals of technical installations, with typical frequencies of 50 or 60 Hz (AC power) or 16.7 Hz (German railway system), are expected to be lower for (E_z) receivers located within observation boreholes than for (horizontal) electric field recordings at surface.

In the following, we will present a newly developed modular sensor chain designed for measurement of the vertical electric field in observation boreholes on land. In particular, we will analyse field data obtained with the new sensor in four time-lapse CSEM surveys in North Germany and present a first study of the repeatability of E_z measurements.

2 THE BOCKSTEDT OIL FIELD AND RESERVOIR MONITORING CONSIDERATIONS

The Bockstedt oil field is located in NW Germany (Fig. 1) at the northern edge of the Lower Saxony Basin, which is the most important oil province of Germany (Betz *et al.* 1987). Reservoir rocks and the nature of traps vary within the basin (Kockel *et al.* 1994).

In the Bockstedt region, basin inversion resulted in strike-slip deformation and pop-up/flower structures (*cf.* Leonhardt *et al.* 2011). The reservoir sequence is about 10 m thick and located at about 1200 m depth. Overall, the Bockstedt oil field covers an area of about 0.8×3 km^2 (the shaded ellipse in Fig. 1). More detailed description of the oil province and the regional geology can be found in Kockel *et al.* (1994) and Ziegler (1987), respectively.

The onshore oil field was discovered in 1954 and has been on stream ever since; until today more than 80 wells have been drilled. Following natural oil production (primary oil recovery), re-injection of produced reservoir water and tertiary production trials with polymers have been used to increase recovery rates. In Bockstedt, injected brines (highly saline formation water with or without polymer) usually have much lower electrical resistivity than the oil phase in the reservoir.

The potential of monitoring changes in reservoir oil saturation with CSEM measurements was investigated based on a conceptual reservoir structure by Tietze *et al.* (2015). Background resistivities vary in the upper ∼2000 m in the Bockstedt region between 1 and 10 Ωm and strongly attenuate the EM signal. Numerical simulations considering a conceptual reservoir of $1000 \times 1000 \times 15$ m^3 showed that even a non-physical depletion scenario featuring a decrease of oil saturation from 80 per cent (16 Ωm) to 0 per cent (0.6 Ωm) within the entire volume cannot be detected using only conventional surface-based sources and receivers. Sensitivity increases significantly if sources and/or receivers can be placed in boreholes closer to the reservoir. Modelling results for configurations using alternative source configurations combining vertical and horizontal dipoles and/or receivers measuring the vertical electric field component E_z showed time-lapse differences of more than 10 per cent.

In the Bockstedt oil field, however, actual compartment sizes are smaller and production rates measured after repeated injections suggest that reservoir oil saturation did not change significantly during the time frame of our observations. Detectable variations in reservoir resistivity are, therefore, unlikely to have occurred, which means any time-lapse differences of our CSEM data are well below 1 per cent. On the positive side, these mostly stable reservoir conditions provide an unprecedented opportunity to investigate the repeatability of CSEM measurements under *in situ* conditions including novel source and receiver configurations.

For a CSEM survey (5 transmitters, 29 receivers; locations see Fig. 1) in May 2014, we successfully deployed and tested a novel horizontal–vertical source for which current is injected via the steel casing of a 1.3 km deep abandoned oil well (Tietze *et al.* 2015). As a first repeatability test, measurements including the novel borehole source were carried out again after 10 d and most observations agreed within 1–2 per cent. Between these measurements, receivers and transmitter current electrodes were left in place.

In the following, we compare data of the 2014 survey with further repeat measurements carried out across the Bockstedt oilfield in 2015, 2016 and 2018 (see Section 4). Starting in 2015, the recordings included a newly developed sensor chain recording the vertical electric field in a 200 m deep observation well (see Section 3).

3 A NOVEL RECEIVER CHAIN TO MEASURE THE VERTICAL ELECTRIC FIELD

Key components of the new tool to measure the vertical electrical field in shallow observation boreholes are plastic-made sensor modules that hold non-polarizing telluric electrodes and steel-coated
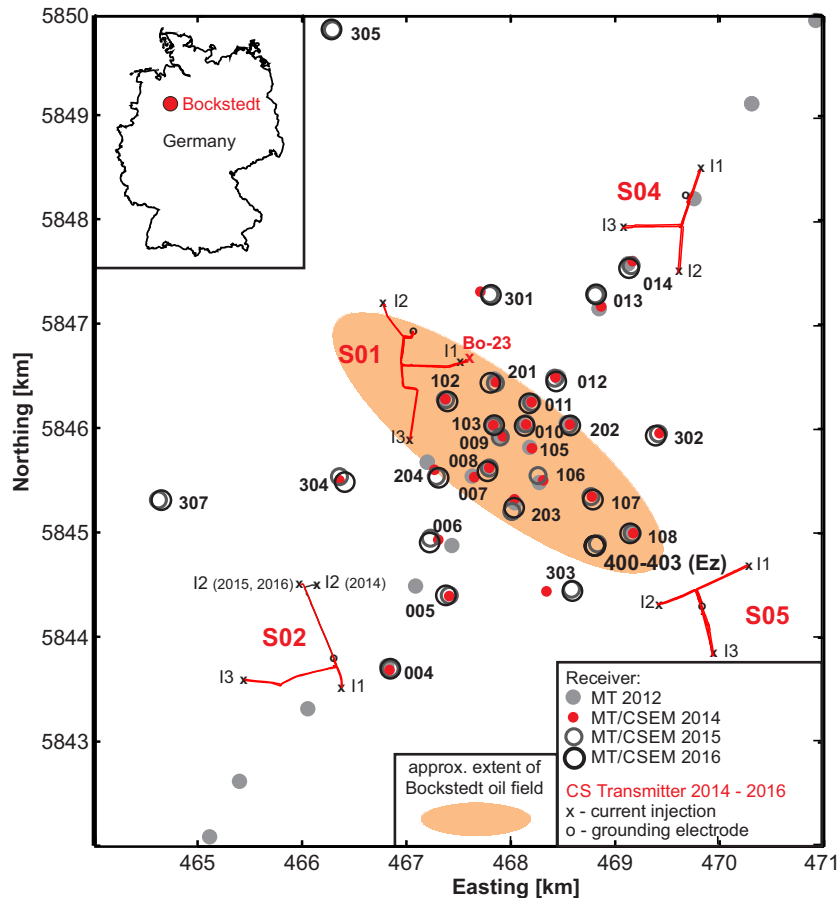
Figure 1. Location of CSEM/MT receiver stations (red symbols) and CSEM transmitters (red lines and black symbols) deployed during the CSEM main surveys at Bockstedt in 2014–2016. The observation well equipped with three E_z receivers is located at receiver position 400–403 at the southeastern edge of the oilfield. At each transmitter location, current was injected through three grounded electrodes (steel rods, black crosses, labelled I1, I2, I3). The red lines show cables that connected the electrodes to the signal generator. Signal and power generator were located at the centre of the transmitter layout next to the grounding electrode (black circle). At transmitter S01, one of the grounded electrodes was replaced with the steel casing of Bo-23 for current transmission. The shaded ellipse marks the approximate horizontal extent of the oil reservoir. Inset in top left corner shows location of the survey area within Germany.

multiwire logging cable that holds the sensor chain, controls sensor spacing and transfers analogue signals to the data logger.

Each sensor unit (Fig. 2a) comprises a redesigned slimmer version of the Ag/AgCl electrodes designed and manufactured by GFZ Potsdam (www.gfz-potsdam.de/gipp), which is incorporated into a cylindrical torpedo-shaped plastic enclosure to allow for deployment in boreholes. Galvanic contact with surrounding fluids is ensured via holes (perforation) in the enclosure (bottom panel in Fig. 2a). Several synthetic materials were tested but eventually we decided to use Polyoxymethylen for its high stiffness, low friction and excellent dimensional stability at affordable costs. The sensor unit has a length of 0.76 m and a diameter of 90 mm, thus fitting many standard oil or water well casings.

The sensor units are connected with a standard multiwire logging cable (signal wires inside and steel coating outside). Segments of the borehole cable are connected at the top and bottom of each E_z sensor using rope sockets (middle panel in Fig. 2a). All signal wires are continuous within the E_z sensors and throughout the receiver chain. A weight, provided as a separate unit, is attached at the bottom of the logging cable, to ensure a reasonable sinking speed of the entire sensor chain (Fig. 2b).

Position of sensor units along the receiver chain is simply determined by the lengths of cable segments. As both the mechanical

and the signal connections can be (un)plugged at top/bottom of each sensor unit, the configuration of the entire sensor chain can easily be varied using interconnecting cable segments with different lengths.

In September 2015, a sensor chain equipped with three borehole electrodes was installed in a 208 m deep, newly drilled observation borehole in the southeastern part of the survey area (Fig. 2b; see Fig. 1 for borehole location). Borehole electrodes are located at depths of 92, 140 and 188 m, respectively. The entire sensor chain weighs approximately 150 kg. The borehole is stabilized with a PVC casing, which is slotted along three segments of 12 m lengths centred on the receiver positions (grey shaded sections in Fig. 2b) to allow galvanic contact with surrounding formations. A behind-casing filling with quartz sand prevents infiltration of sediments into the borehole. After drilling, an open-hole log was run measuring deviation from vertical, calibre and gamma ray. Overall, deviations from verticality are in the order of only a few centimetres over 200 m, which makes the borehole nearly vertical.

For measuring the vertical electric field, we also installed conventional, non-polarizing Ag/AgCl-electrodes (sensor 0 in Fig. 2b) as a reference at surface. As the cellar around the borehole is cemented,
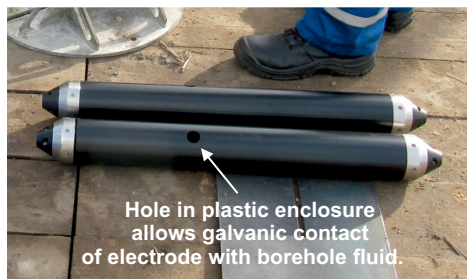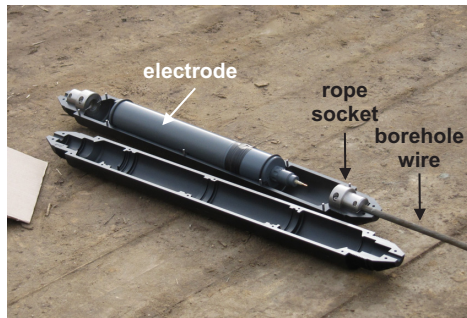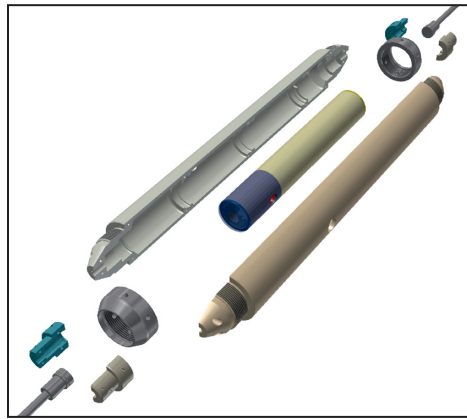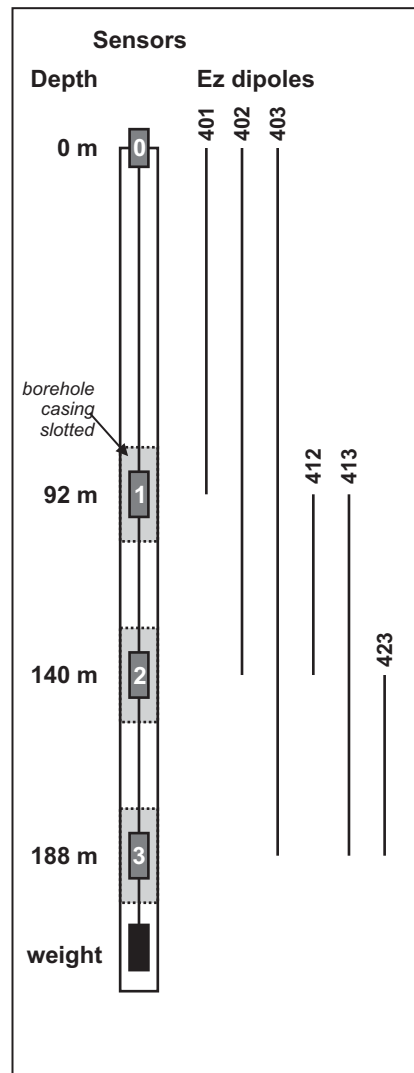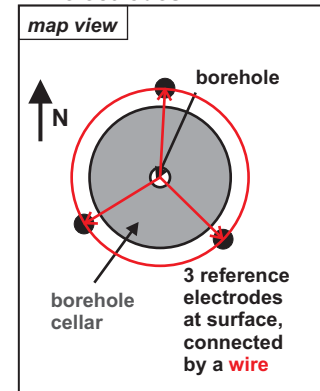
Figure 2. Modular E_z receiver chain. (a) Electrode modules consisting of plastic enclosure and Ag/AgCl electrodes. Modules are connected via borehole cables (internal wiring missing in sketch and photos). For a detailed description see main text. (b) Sensor configuration within observation borehole in the Bockstedt oil field and E_z measuring dipoles (see Fig. 1 for borehole location). The electrodes of the receiver chain (1–3) are centred at 92, 140 and 188 m below surface, respectively. In the field, time-series of dipoles 0401–0403 measuring the electric field between surface and borehole electrodes 1–3, respectively, were recorded. Time-series for dipoles 0412–0423 can be obtained by subtraction of recorded data. (c) Configuration of electrodes at surface since October 2015 (map view).

the surface electrodes could only be placed at ∼1 m horizontal distance from the borehole centre. To simulate a reference electrode centred above the borehole, we installed a set of three interconnected electrodes (Fig. 2c), distributed equidistantly around the borehole centre. With this set-up, horizontal electric field components between surface and borehole electrodes are expected to cancel out and the recordings should contain only the vertical electric field. The three surface electrodes were buried as long-term installations following a concept that was developed for electric field recordings at permanent MT stations (Ritter *et al.* 2015; Araya & Ritter 2016). All electrodes of the E_z receiver, in the borehole and at surface, were left in place since their first installation in September and October 2015. The surface electrode served as reference for all three E_z receivers, thereby establishing three vertical dipoles (401–403 in Fig. 2b).

4 CONTROLLED-SOURCE ELECTROMAGNETIC TIME-LAPSE SURVEYS ACROSS THE BOCKSTEDT OIL FIELD 2014–2018

4.1 Survey layout and recording modes

Between May 2014 and November 2016, three CSEM surveys (5 transmitters, 29 receiver locations; Fig. 1) were carried out across the Bockstedt oil field, including a novel borehole-surface source, whereby the current is injected via the steel casing of a 1.3 km deep abandoned oil well (Tietze *et al.* 2015). For the 2015 and 2016 repeat surveys, set-up of transmitters and receivers was kept as close as possible to the original deployment of 2014 (Fig. 1). For the majority of transmitter and receiver points, we could accomplish a

redeployment within ∼10 m of the original positions for all three field campaigns. The newly developed borehole sensor for measuring the vertical electric field (*cf.* Section 3) was installed in 2015 and vertical electric field recordings are available for the 2015 and 2016 field surveys (see Fig. 1 for borehole location).

The new vertical source/receiver components were used in combination with a more traditional CSEM set-up. A three-phase CSEM transmitter of GFZ Potsdam (Streich *et al.* 2011) was deployed for current injection at four locations (S01–S05; red lines in Fig. 1) in all surveys. Each transmitter consists of two electric dipoles (actually a tri-pole with programmable current polarizations) and currents are injected using four steel rods (one at the centre and three at the cable ends), which are driven into the ground. For the repeat surveys, 14 of the 16 steel rods could be relocated within ∼10 m of the 2014 positions. Injection point S01-I3 (see Fig. 1) was shifted by ∼20 m for logistical reasons; steel rod S02-I2 had to be moved by ∼100 m to the west (see Fig. 1) for safety reasons, to avoid crossing a road with cable bridges.

At transmitter S01, the standard layout consisted of the three grounded steel rods *I1*, *I2* and *I3* (S01-S) and alternatively, steel rod *I1* was replaced by the steel casing of the abandoned oil well Bo-23 (S01-Bo; Tietze *et al.* 2015). Steel rod and the surface location of the Bo-23 oil well are approximately 50 m apart (∼east–west direction). At each source position, we transmitted square wave signals with base frequencies between 16 and 0.0156 Hz (S01-Bo, S02, S04, S05) or 0.03125 Hz (S01-S) for all three source current polarizations. Period range of transmission and duration of current injection was kept the same for all field campaigns. When using the abandoned oil well (I1 of S01-Bo) with its low contact resistance <1Ω, we were able to inject the maximum possible current of 40 A. For all other transmitter electrodes, we usually achieved current strengths between 15 and 35 A, which varied between the three electrodes of each transmitter as well as between years. Accuracy of current measurements is <± 1 per cent.

24–25 surface receivers were deployed across the Bockstedt oil field at 29 locations (004–400; Fig. 1). At 21 of these receiver locations, instruments could be deployed in all surveys, with relocation errors ranging from <10 m (13 stations) to 270 m (Fig. 1). Relocation distances >40 m occurred only between the 2014 and 2015 surveys and were mostly due to unforeseeable circumstances, such as denial of land access, construction of new windmills or postponed harvesting activities. In 2016, all receiver stations could be redeployed within 40 m of the 2015 positions.

In all surveys, two pairs of electrodes in N–S and E–W direction were deployed at all receiver stations to measure the horizontal electric field. In 2014, all stations were additionally equipped with three induction coil magnetometers in N–S, E–W and vertical direction. As modelling and inversion of CSEM data suggested that magnetic fields provided little additional information along with the electric fields (Tietze *et al.* 2015), the number of stations with magnetic sensors was reduced to 11 and 10 for surveys in 2015 and 2016, respectively. Here, we will only consider the electric fields.

We used the S.P.A.M. MkIV data loggers of the Geophysical Instrument Pool Potsdam to record time-series of electric and magnetic fields (receiver) as well as injected currents (transmitter). Data were collected continuously with a sampling frequency of 500 Hz over the entire survey time. In addition, receiver data were recorded with higher sampling rates at various intervals (e.g. sampling with 25 kHz for 10 min at 00:00 UTC; 10 min with 1250 Hz every 2 hr). Natural source MT data were collected at times when the current source was not in operation, for example, at night.

All receivers were installed within the first days of the surveys and typically recorded throughout the entire survey. Transmitters were deployed sequentially beginning after receivers had been installed and operated for 1–3 d. During the surveys, first quality check of the recorded data was conducted using single site MT processing of the night recordings of the data, that is, times when the transmitter was off. Data recovery rates varied between about 98 per cent for the 2014 and 2016 field campaigns and 90 per cent for the 2015 survey. Higher instrument failure in 2015 was related to a software problem and more frequent damage of cables by animals.

The sensor chain developed in the framework of this project (see Section 3) to measure the vertical electric field (E_z) was installed about 2.5 km SE of transmitter S01 (see Fig. 1 for location). For preliminary measurements of the vertical electric field directly after installation in September 2015, we temporarily installed only one conventional, non-polarizable Ag/AgCl-electrode (electrode 0 in Fig. 2b) at surface directly next to the concrete borehole cellar, that is, ∼1 m southeast of the borehole centre. Because the surface electrode serving as reference for all three electrodes at depth (dipoles 401–403 in Fig. 2b) was shifted from the centre position, all three dipoles were not perfectly vertical but contained a horizontal component in SE direction.

At the beginning of the main CSEM survey in October/November 2015 the permanent installation with three surface electrodes was established (see Section 3). Contact resistances of borehole electrodes were determined at the beginning of each survey to confirm integrity of the sensors measuring 200–500 Ω (October 2015), 200–900 Ω (March 2016), 500–900 Ω (October 2016) and ∼10 kΩ (May 2018). Over time, contact resistances increased. Yet, values are in a similar range as for conventional, temporarily installed surface electrodes in the survey area.

For comparison, a 5-channel receiver station recording horizontal electric and three-component magnetic fields was deployed at surface as close as possible to the borehole location (site 400) during measurements in 2015 and 2016.

In the course of the project, three short-time test surveys (each about 1 week) were conducted to investigate integrity of the E_z receiver. For these tests, currents were injected only at transmitter S01-Bo. For comparison, horizontal electric fields were recorded at receivers 202 (2015, 2016, 2018), located about 1 km north of the observation well, and 400 (2016, 2018), situated at the observation borehole.

4.2 Data processing (CSEM transfer functions)

For interpretation, we process the CSEM data as transfer functions (TFs) using the robust algorithm of Streich *et al.* (2013) for all source–receiver combinations. TFs relate the three tri-pole source currents of each wire (*I1, I2, I3*) to the EM fields (e.g. E_x, E_y, E_z) recorded at the receivers. As the three currents I_k have a constant phase shift of 120°:

$$I_k = I(\omega)\cos((k-1) \times 120° + \varphi);\ k\epsilon\,(1, 2, 3),\qquad(1)$$

the sum of the currents (*I1, I2, I3*) injected through the three grounded electrodes is zero at all times. Therefore, any field component in the frequency domain can be represented in terms of two source currents:

$$\begin{pmatrix} E_x \\ E_y \\ E_z \end{pmatrix} = \begin{pmatrix} T_{13}^{E_x} & T_{23}^{E_x} \\ T_{13}^{E_y} & T_{23}^{E_y} \\ T_{13}^{E_z} & T_{23}^{E_z} \end{pmatrix} \begin{pmatrix} I_1 \\ I_2 \end{pmatrix}.\qquad(2)$$

The elements T_{ij} of the matrix relate source currents to the observed field components with respect to amplitude and phase. They are frequency-dependent TFs that contain information on the subsurface conductivity but also depend on the source geometry. In total, there are three possible combinations of source currents each associated with two response functions. Note, only two of the six response functions are independent as $T_{ij} = -T_{ji}$ and because each TF can be reconstructed from two other TFs, for example, $T_{23} = T_{13} - T_{12}$. Estimates of TFs are obtained using a robustly weighted least-squares fitting. Uncertainties of each element T_{ij} are provided as 2×2 covariance matrix. In the following, we use the standard deviation of each element (i.e. the square root of the variances/diagonal elements of the covariance matrix) as a measure of uncertainty or, in return, data quality.

Streich *et al.* (2013) showed that linear combinations of TFs obtained from processing can be used to synthesize responses for arbitrary source polarization angles φ (*cf.* eq. 1). In fact, TFs T_{12}, T_{13} and T_{23} only differ by a scaling factor from fields that would be measured for specific angles φ. For example, for $\varphi_1 = 30°$ the field F (any component of the electric or magnetic fields) is given by

$$(F(\varphi = 30°)) = I\left(\sqrt{3}/2\right) \cdot T_{12}^F. \tag{3}$$

Similarly, TFs T_{13} and T_{23} are related to fields for source polarizations of $-30°$ and $-90°$, respectively. For clarity, TFs are written without sub or superscripts in the following using the pattern T*ij*-F instead of T_{ij}^F. For example, T_{13}-E_x stands for $T_{13}^{E_x}$.

In the Bockstedt oil field, cultural EM noise at frequencies of 50 and 16.7 Hz is very significant across the survey area. Hence, time-series of recorded data were notch-filtered to remove these two frequencies and their harmonics prior to CSEM processing. CSEM processing parameters were based on recommendations provided in Streich *et al.* (2013), yet we did not apply a windowing (taper) function prior to FFT.

5 QUALITY AND REPEATABILITY OF CSEM MEASUREMENTS

In the following, CSEM data quality and repeatability for the Bockstedt CSEM data sets are examined based on the TFs estimates (*cf.* Section 4.2). Fig. 3 illustrates TFs of the Bockstedt data set exemplarily for two source–receiver combinations. In general, amplitudes and phases of TFs in Figs 3(a) and (b) vary smoothly with frequency, as can be expected for physically consistent data. Absolute values of TF amplitudes are primarily determined by the amplitude behaviour of the CSEM source field, that is, the source–receiver geometry. For receiver 204, located within 500 m of the southern injection point of transmitter S01-Bo (see map in Fig. 1), TF amplitudes reach up to 10^{-5} V A^{-1} m^{-1} (Fig. 3a), whereas at receiver 004 (2.5 km south of transmitter S01-Bo) amplitudes of T_{12}-E_x (see Section 4.2 for labelling TFs) are as low as $\sim 2 \times 10^{-9}$ V A^{-1} m^{-1} for frequencies of 1 Hz (Fig. 3b).

Results in Fig. 3(a) also show that TF magnitudes can differ by several decades even between TF components (T_{12}-E_x, T_{13}-E_x, T_{23}-E_x) and frequencies at a particular receiver position. Moreover, Figs 3(a) and (b) illustrate that each TF can be reconstructed from two other TFs, for example, $T_{23} = T_{13} - T_{12}$ (*cf.* Section 4.2). At receiver 204 (Fig. 3a), for example, TFs T_{13}-E_x (circles) and T_{23}-E_x (diamonds) have very similar amplitudes and symbols lie on top of each other. Accordingly, T_{12}-E_x (triangles) which represents the difference between the other two components is about two orders of magnitude smaller over wide parts of the frequency range.

The error bars in Fig. 3 illustrate standard deviations of TF amplitudes and phases obtained from bivariate robust frequency-domain processing (*cf.* Section 3.2), which are used as a data quality measure in the following.

5.1 Quality of CSEM data and variability over time

At first, statistical distribution of TFs and associated uncertainties (standard deviation) obtained from processing (Streich *et al.* 2013; see Section 4.2) are considered to obtain an overall idea of CSEM data quality for the Bockstedt oil field for each survey but also over time. The uncertainty estimates provide a measure of the total EM noise, including the measuring system and the environment of source and receiver during the measurement time within a particular survey (usually ∼14 hr per transmitter location/year, *cf.* Section 3.2).

In order to study signal-to-noise ratios, 2-D heatmaps in Figs 4(a)–(c) illustrate occurrence rates of standard deviations of TF amplitudes versus TF amplitudes colour-coded for the three surveys. Colour intensity specifies the statistical frequency (significance) and the colouring indicates (dis)similarity between measurements of the three campaigns. If the signal-to-noise ratios (distributions) of all three campaigns are identical, pixels assume a grey colouring. Red, blue or green shading occurs if bin counts are dominated by one of the surveys, that is, the 2014, 2015 or 2016 survey, respectively. The lines in Figs 4(a)–(c) mark relative uncertainties of 100–0.01 per cent of TF amplitudes.

Results are displayed for all five transmitters (Fig. 4a), transmitters S01-Bo (Fig. 4b) and S04 (Fig. 4c). Overall, TF amplitudes of horizontal electric fields for both transmitters range from 10^{-4} to 10^{-10} V A^{-1} m^{-1} (horizontal extent of cluster in Fig. 4a) and their uncertainties vary between 10^{-7} and $10^{-10.5}$ V A^{-1} m^{-1} (vertical extent of cluster in Fig. 4a).

Amplitudes of CSEM fields (and thus TFs) are dominated by the source–receiver distances. Highest TF amplitudes are found at receivers closest to the source; lowest amplitudes are measured at sites with largest distances. For transmitter S01-Bo located in the centre of the survey area, source–receiver distances vary between ∼0.5 and 3.7 km and related TF amplitudes range from 10^{-5} to 10^{-8} V A^{-1} m^{-1} (Fig. 4b). For transmitter S04 located at the northern edge of the survey region (and similarly for transmitters S02 and S05), source–receiver distances measure up to 6 km with nearly all receivers located at ≥2 km distance. Hence, TF amplitudes of this transmitter (Fig. 4c) are overall smaller ranging from 10^{-6} to 10^{-9} V A^{-1} m^{-1} except for two receivers located at only 0.5 (014) and 1.2 km (013) distance.

Results in Figs 4(a)–(c) reveal that characteristics of the uncertainties change with TF amplitudes. For TFs with amplitudes $<10^{-7}$ V A^{-1} m^{-1}, uncertainties cluster between 10^{-9} and 10^{-10} V A^{-1} m^{-1} independent of TF amplitudes corresponding to relative errors of 0.1–10 per cent with a focus at 1 per cent (dark colours in Figs 4b and c). For TFs with amplitudes $>10^{-7}$ V A^{-1} m^{-1}, however, errors rise proportionally with the TF amplitudes with the majority 'following' the 0.1 per cent line (Figs 4a and c). In other words, highest data quality is obtained close to the sources and signal-to-noise ratios decrease with growing source–receiver distances.

We speculate that for the lower end of the TF amplitude range ($<10^{-7}$ V A^{-1} m^{-1}), errors are dominated by 'external' EM noise from cultural installations and natural EM field variations (such as the MT signal) that is independent of the measured CSEM signal. Electric field measurements for the Bockstedt region at times when
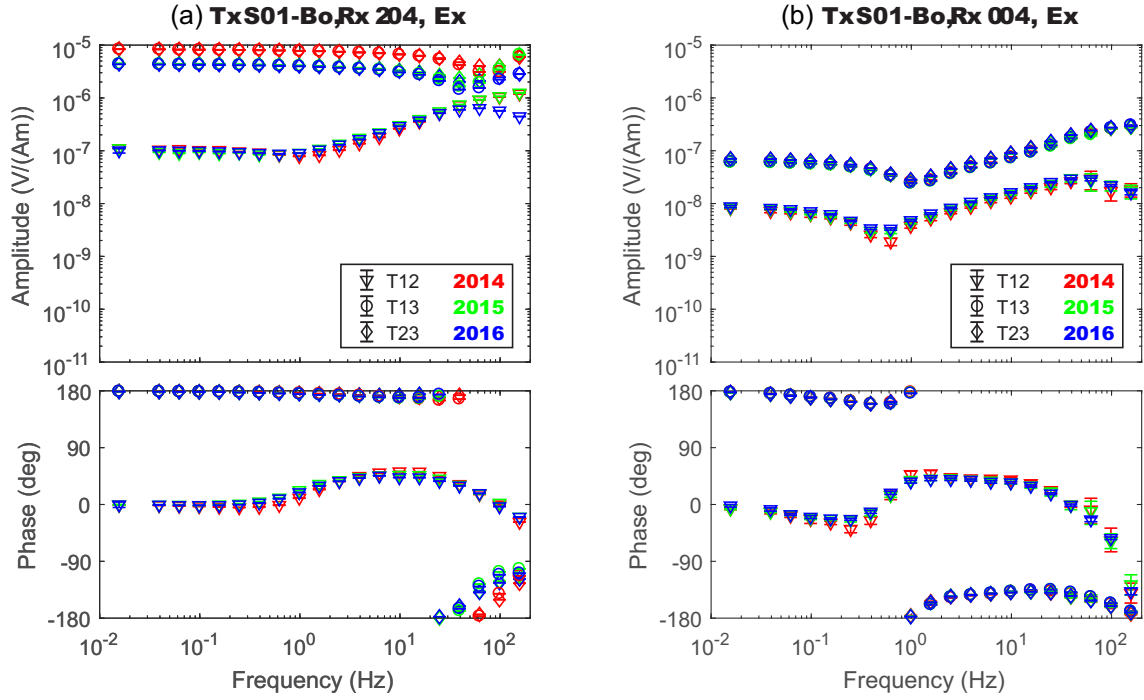
Figure 3. Comparison of transfer functions (symbols) obtained for transmitter S01-Bo during the three main surveys (symbol colour). (a) Receiver 204 located at 500 m distance from the southern electrode I3 of transmitter S01-Bo and (b) receiver 004 located 2.5 km south of transmitter S01-Bo.

the transmitter was switched off suggested EM noise levels stable over time (2012–2014; Tietze *et al.* 2015) with spectral amplitudes between 10^{-9} and 10^{-11} V m^{-1} for the frequency range of 0.0156–200 Hz. Considering transmitter currents in the range of 10 A, error levels of 10^{-9}–10^{-10} V A^{-1} m^{-1}, as observed for low TF amplitudes, are in general agreement with these expectations.

The second noise source is intrinsic and comprises all components of the measuring system, including transmitter and receiver instrumentation noise, variations in transmitter currents and contact resistances, and data processing procedures. Hardware noise is in general considered proportional to signal amplitudes (e.g. Constable 2010). In the Bockstedt area, this 'system noise' appears to become significant for TFs with amplitudes $>10^{-7}$ V A^{-1} m^{-1} for which we obtain a lower error bound of $\sim$0.1 per cent and it dominates the errors for amplitudes $>10^{-6.5}$ V A^{-1} m^{-1}.

Above considerations on noise sources are supported when examining the frequency dependence of the TF errors. Figs 4(d) and (e) show histograms of amplitude errors versus TF frequency again colour-coded for the three main surveys. Errors of TFs with amplitudes $>10^{-7}$ V A^{-1} m^{-1} in Fig. 4(d) associated with 'intrinsic noise' appear nearly constant over frequency with a slight increase towards higher frequencies (>10 Hz). In contrast, for TFs with amplitudes $<10^{-7}$ V A^{-1} m^{-1} uncertainties show a clear variation with frequency (Fig. 4e). For the lowest (<0.3 Hz) and highest (>10 Hz) frequencies, amplitude uncertainties focus around 10^{-9} V A^{-1} m^{-1}, in between amplitude errors decrease to $\sim 2 \times 10^{-10}$ V A^{-1} m^{-1}. This trend strongly resembles the variation of spectral amplitudes of electric fields observed by Tietze *et al.* (2015) at times when the transmitter was switched off (see fig. 4 in Tietze *et al.* 2015). Hence, 'external noise' is considered the main noise source at amplitudes $<10^{-7}$ V A^{-1} m^{-1}. Consideration of these two noise sources is important to establish the general framework for repeatability of CSEM measurements and monitoring at a certain location.

Overall, predominantly grey colouring in Figs 4(a)–(c) shows that the overall distribution of amplitudes and errors is consistent for all surveys and transmitters, that is, constant over time. The blue shading towards the bottom of the clusters in combination with the red and green shading at the top suggests that overall quality of the 2016 data set (blue) is slightly higher than for 2014 (red) and 2015 (green). Highest data quality in the Bockstedt area can be expected at frequencies between 0.1 and 10 Hz, which coincides with the frequency range considered most important/suitable for monitoring a reservoir scenario as in Bockstedt (Tietze *et al.* 2015).

5.2 Repeatability of horizontal electric fields at surface

In order to study the repeatability of CSEM measurements, that is, the stability of measurements over time spans of several months or years, we consider differences between TF estimates obtained for the three CSEM surveys. In particular, we investigate the time-lapse periods between the 2014 and 2015 as well as the 2015 and 2016 measurements:

$$\Delta_{\text{abs}} = \left| T_{ij}\text{-}F\,(\text{year2}) \right| - \left| T_{ij}\text{-}F\,(\text{year1}) \right|, \tag{4}$$

$$\Delta_{\text{rel}} = \left(\left| T_{ij}\text{-}F\,(\text{year2}) \right| - \left| T_{ij}\text{-}F\,(\text{year1}) \right| \right) / \left| T_{ij}\text{-}F\,(\text{year1}) \right|, \tag{5}$$

$$\Delta_{\text{phs}} = \arg\left(T_{ij}\text{-}F\,(\text{year2}) \right) - \arg\left(T_{ij}\text{-}F\,(\text{year1}) \right), \tag{6}$$

where T_{ij}-F is the TF component T_{ij} (T_{12}, T_{13}, T_{23}) of receiver channel F (E_x, E_y, E_z), year1 and year2 (year1 < year2) are survey years, Δ_{abs} and Δ_{rel} are the absolute and relative differences between TF amplitudes, respectively, and Δ_{phs} is the absolute difference of TF phases. We confine the phases of complex TFs and corresponding phase differences Δ_{phs} to the interval between $-180°$ and $+180°$.
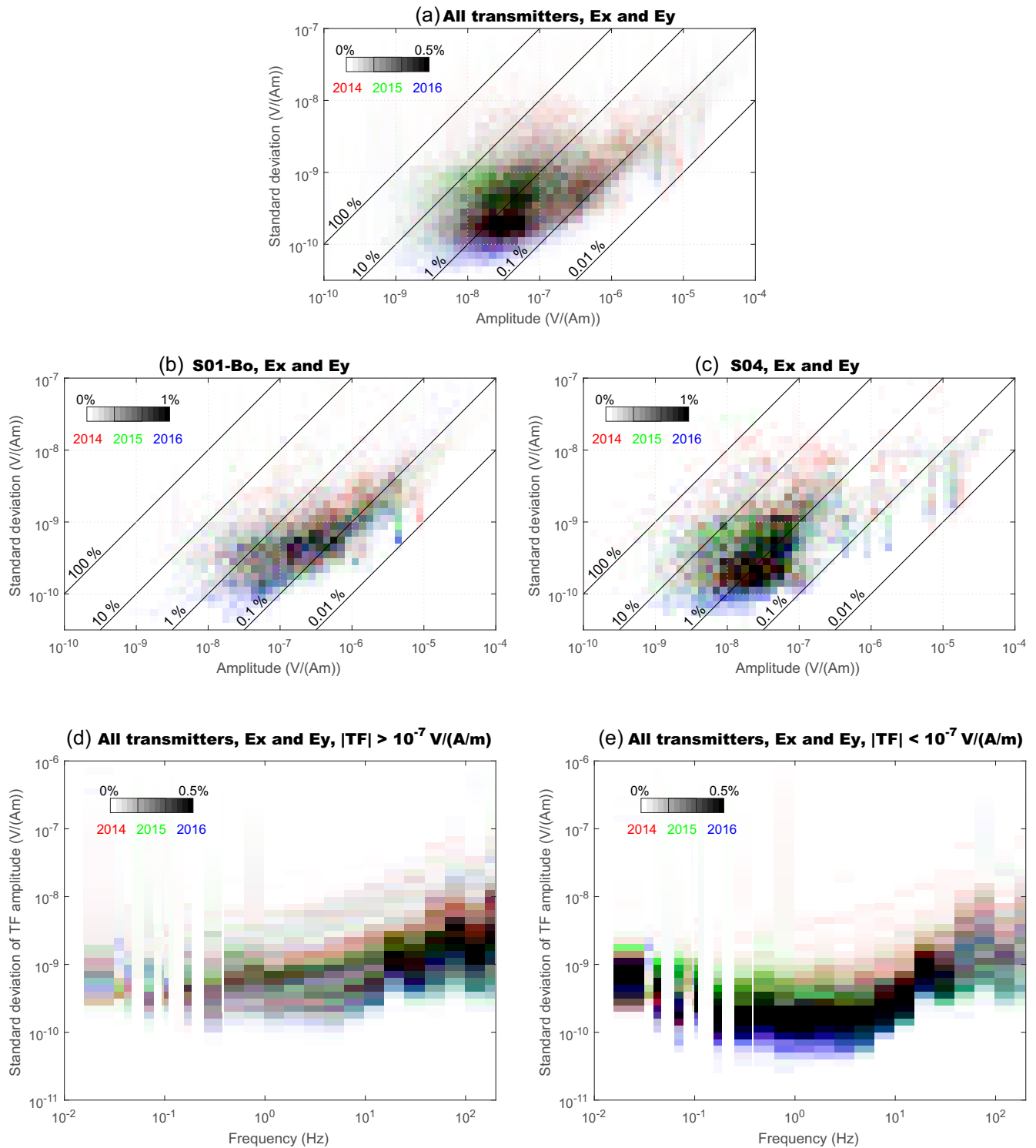
Figure 4. Analysis of TF uncertainties (standard deviations). (a–c) Heatmaps of standard deviations of TF amplitudes versus TF amplitudes for horizontal electric fields colour-coded for the 2014 (red), 2015 (green) and 2016 (blue) surveys for various transmitters. Analysis includes TFs T_{12}, T_{13} and T_{23} for both E_x and E_y. Fully saturated pixels correspond to occurrence rates of ≥ 1 per cent (a and b) and ≥ 0.5 per cent (c), respectively. The diagonal lines in (a)–(c) mark uncertainty-to-amplitude ratios of 100–0.01 per cent. (a) Transmitter S01-Bo, (b) transmitter S04 and (c) all transmitters. (d and e) Heatmaps comparing standard deviations of TF amplitudes versus TF frequency using the same colour coding as in (a)–(c). Fully saturated pixels correspond to occurrence rates ≥ 0.5 per cent. (d) TF amplitudes $> 10^{-7}\,\mathrm{V\,A^{-1}\,m^{-1}}$, (e) TF amplitudes $< 10^{-7}\,\mathrm{V\,A^{-1}\,m^{-1}}$.

In the following discussions, Δ_{abs} will be referred to as absolute difference or absolute change of the TF amplitude during a time-lapse period; analogue expressions will be used for Δ_{rel} and Δ_{phs}.

Standard deviations of TFs given by the processing routines provide a measure of EM noise of the measuring system and the environment of source and receiver during the measurement time within a particular survey. Here, we use these uncertainties in combination with error propagation procedures to derive uncertainty estimates for differences of TFs (eqs 4.1–4.3). These derived error estimates capture uncertainties resulting from the two independent, noise-affected measurements assuming identical surveying parameters. However, they do not represent a measure for deviations between surveys that result from differences in station set-up (such as sensor misalignment; *cf.* Supporting Information) or changes of the resistivity distribution in the subsurface. Identifying the latter is of course the primary objective of monitoring applications.

For the Bockstedt data sets, sizeable resistivity changes can be ruled out for the reservoir region (*cf.* Section 2). For logistical reasons, instrumentation could only be (re-)installed temporarily for each of the field campaigns and despite great efforts of all involved parties to replicate previous survey positions, differences in installation positions reached up to 250 m for receivers between the 2014 and 2015 surveys and up to 40 m between the 2015 and 2016 surveys (*cf.* Fig. 1 and Section 4.1).

Small changes in the survey configuration can have measurable influence since CSEM source fields have strong spatial gradients. 1-D simulations for the Bockstedt configurations of 2014–2016 showed that changes on the order of a few tens of metres can already change TF amplitudes by more than 20 per cent (Supporting Information Figs S1 and S2). In general, the influence of survey layout alterations on TF amplitudes and phases depends not only on the spatial relocation distance between the observation points but also on the CSEM field distribution, that is, on the survey layout and the underlying conductivity structure. Therefore, relocation of stations affects each combination of TF component, receiver and transmitter in a different way. As the true layout of receivers and/or transmitters is part of the modelling procedures, time-lapse data obtained with modified receiver and/or transmitter layout can in general be fully considered at that stage of the interpretation (inversion). But for a direct comparison of CSEM data acquired in a time-lapse manner without any modelling, that is, as differences or ratios between TFs, relocation of receivers and transmitter electrodes must not exceed a few (tens of) metres (Supporting Information Fig. S2).

Here, receivers with deviations in sensor positions >35 m are excluded from considerations in the following. Hence, analysis of TF differences between the surveys can be understood as an estimate of measurement errors introduced by minor (<40 m) relocation errors and resistivity variations outside the reservoir, such as seasonal variability near the surface, at least in the Bockstedt survey area.

Fig. 5 provides a first overview on the characteristics of TF variations occurring within the two time-lapse periods. The colour-coded heatmap in Fig. 5(a) compares TF amplitudes with amplitude differences for both time-lapse periods. Overall, amplitude differences for both the 2014–2015 (green) and the 2015–2016 (blue) time-lapse periods cover a range between 10^{-10} and 10^{-5} V A^{-1} m^{-1} (vertical extent of cluster in Fig. 5a). Time-lapse changes appear proportional to TF amplitudes and vary between 0.1 and 100 per cent of the amplitudes (the solid lines in Fig. 5a). For 50 per cent of the data points, relative differences between subsequent measurements is ≤4.1 per cent (median; dashed line in Fig. 5a). Differences of TF phases displayed in Fig. 5(b) distribute symmetrically around zero independent of TF amplitudes (horizontal cluster in Fig. 5b). For

90.8 per cent of all data points, phase changes are between ±10°, that is, within the plot, with a median difference/value of ±0.96° (dashed line in Fig. 5b).

In order to evaluate the relevance of the observed changes, Figs 5(c) and (d) compare amplitude and phase differences with their corresponding standard deviations derived by propagation of uncertainty. Amplitude differences between surveys span a wide range between 0.1 and 100σ (the solid lines in Fig. 5c).

In many disciplines, changes of measurements are considered detectable or significant if they exceed 3 standard deviations (3σ or 99.7 per cent level; red lines in Figs 5c and d). Following this approach, 52.0 per cent of amplitude differences and 41.7 per cent of phase differences classify as significant. These numbers appear large at first considering that we do not expect changes in the target structure and may give the impression that monitoring is not possible.

More systematic investigation reveals that these large and significant time-lapse differences do not occur randomly but focus within particular frequency ranges and source–receiver combinations. Figs 6 and 7 show time-lapse changes of selected TFs broken down by frequency (vertical axes in Figs 6 and 7) and by receiver, sorted by radial distance from the transmitter (horizontal axes in Figs 6 and 7). White colours in Figs 6 and 7 indicate absolute and relative amplitude variations $<10^{-9}$ V A^{-1} m^{-1} and $<\pm0.5$ per cent, respectively, and phase variations $<\pm0.5°$. Blue (red) colouring corresponds to an increase (decrease) of respective values over time. Bold outlines mark data points for which time-lapse differences remain within 3 standard deviations (*cf.* Figs 5c and d).

Large differences often occur in TF components with small amplitudes and, thus, weak signal-to-noise ratio. For transmitter S04, T_{13}-E_x is the largest TF component at most sites and about one order of magnitude larger (Fig. 6a, mainly green colours) than the smallest component that is usually T_{12}-Ex (predominantly blue colouring in Fig. 6b). Absolute changes of TF amplitudes between consecutive surveys are on the same order of magnitude for both components (Figs 6c and d). Hence, relative differences (Figs 6e and f) and phase differences (Figs 6g and h) of TF components of the same transmitter but with different polarizations behave differently.

For the strongest component T_{13}-E_x, TF amplitudes usually agree within ±5 per cent at source–receiver distances between 2 and 4 km as indicated by the whitish colouring in Fig. 6(e). Differences >10 per cent dominate at sites located >4 km or very close <2 km to the source. Phases mostly deviate less than ±1° (white colours in Fig. 6g) and differences lie within their uncertainties that is indicated by symbols plotted with the bold frames, for example, for frequencies <20 Hz and source–receiver distances >2 km. In contrast, for the smaller component T_{12}-E_x variations for the same time-lapse period appear larger. Blue and red colouring in Figs 6(f) and (h) illustrates that TF amplitudes and phases of the 2015 and 2016 surveys often differ by more than ±5 per cent or ±3°, respectively, throughout the survey area. Yet, differences of T_{12}-E_x measurements are usually still within the uncertainty interval (bold frames) and reflect poorer signal-to-noise ratio.

Results are dominated by the signal-to-noise ratio, which means increasing source–receiver distances increase differences and uncertainties become larger. Yet, at receivers 014–301 located within 2 km of the source (S04), phase differences and relative amplitude changes are both small ($<\pm3°$ and <5 per cent, respectively), but exceed 3 standard deviations (the thin outlines). Error estimation in CSEM processing accounts for influences of EM and system noise that are usually small compared to the
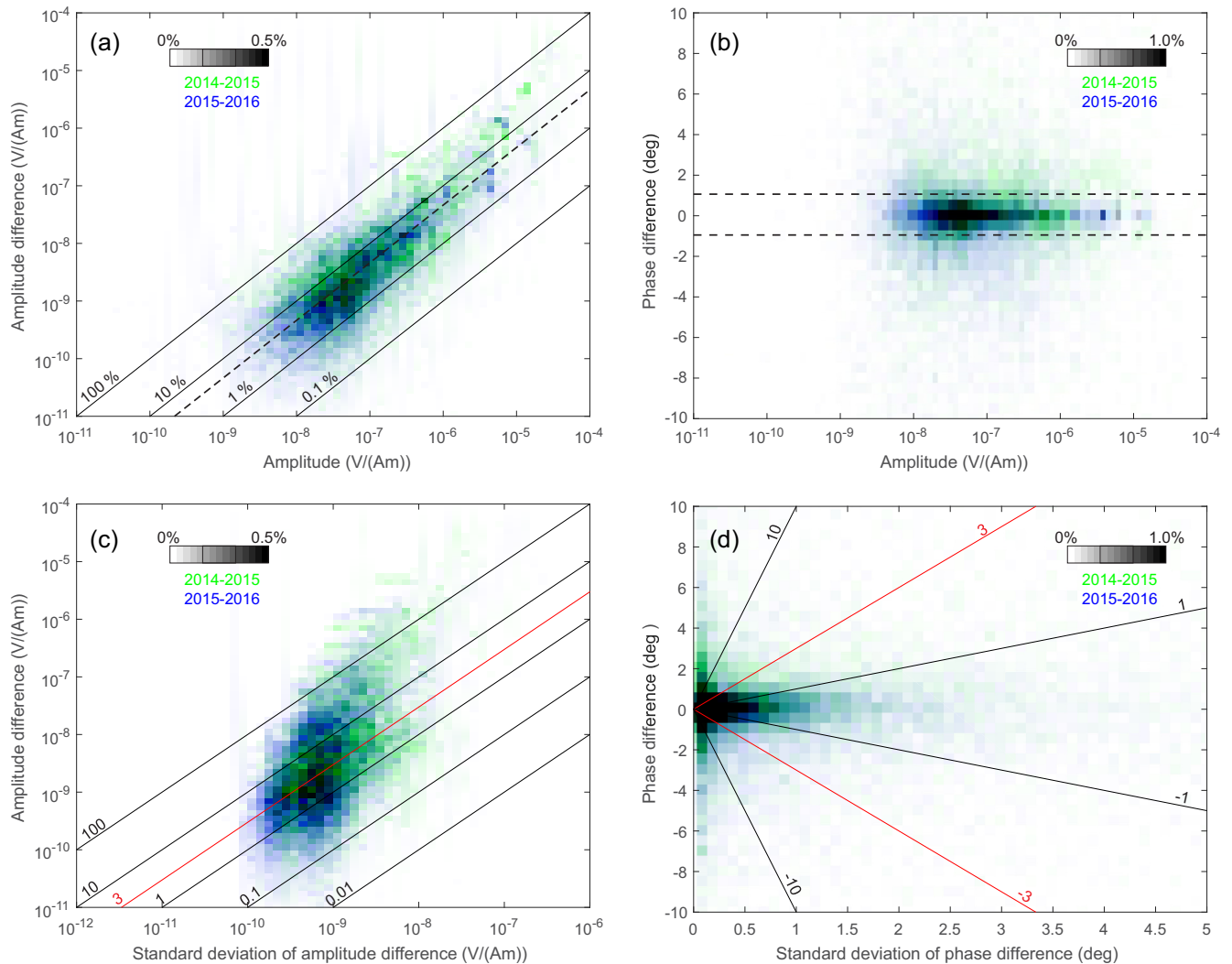
Figure 5. Statistical distribution of time-lapse differences of TFs colour-coded for the two time-lapse periods (green: 2014–2015; blue: 2015–2016). (a–b) Heatmaps comparing differences of (a) TF amplitudes and (b) TF phases to TF amplitudes of the first survey of each time-lapse period. The solid lines in (a) indicate relative amplitude changes of 0.1–100 per cent. The dashed lines in (a) and (b) mark the median of (a) relative amplitude differences and (b) absolute phase differences, respectively. (c–d) Comparison of (c) absolute amplitude differences and (d) phase differences to their respective standard deviations. For uncertainty estimation see main text. The solid lines outline ratio of differences to standard deviations. Differences larger than 3 standard deviations (the red line) are considered significant. Fully saturated pixels correspond to relative occurrence frequencies ≥0.5 per cent (a, c) and ≥1.0 per cent (b, d), respectively.

signal levels close to the source. Hence, time-lapse variations at these receivers probably result from repeatability errors (such as relocation errors) or changes in the near-surface resistivity structure.

The influence of near-surface resistivities on CSEM TFs becomes particularly apparent when considering data of transmitter S05 located in the east of the survey area. T_{23}-E_x is the largest TF at the majority of receivers and demonstrates excellent repeatability for frequencies <20 Hz with TF changes ranging typically <±1° and <1 per cent for phases and amplitudes, respectively. For frequencies >20 Hz, however, results indicate a systematic decrease of TF phases by 2–8° between 2015 and 2016 (red colours in lower panel of Fig. 7a). In contrast, for time-lapse period 2014–2015 phases show increases of 2–5° in this frequency range (blue colours in lower panel of Fig. 7b). Otherwise, differences of amplitudes and phases are generally in the same range for both time-lapse periods. Forward modelling tests using the 1-D model of Supporting Information Fig. S1(a) showed that an increase of near-surface

resistivity by a factor of 2 (e.g. 12–24 Ωm in the upper 10 m) results in phase changes of 2–10° at all receiver stations, while the amplitudes are mostly unaffected. Hence, variations of TF phases at frequencies >20 Hz may be a result of seasonal variations of near-surface resistivity caused by, for example, changes in water saturation and/or temperature of the soil. Similar effects in phases at frequencies >1–10 Hz were also observed for transmitters S01-S and S01-Bo, in particular for the 2015–2016 time-lapse periods (not shown).

In summary, TFs show highest stability close to the source and variability increases with distance between source and receiver, reflecting decreasing signal-to-noise ratios. Large differences >±10 per cent and >±5° occur predominantly for transmitter polarizations with smallest TF amplitudes and at source–receiver distances >4 km. Moreover, TF phases at frequencies >1–10 Hz may be affected by near-surface resistivity changes. Overall, best repeatability was observed for source–receiver distances between 2 and 4 km and frequencies <1 Hz for all transmitters. In particular,
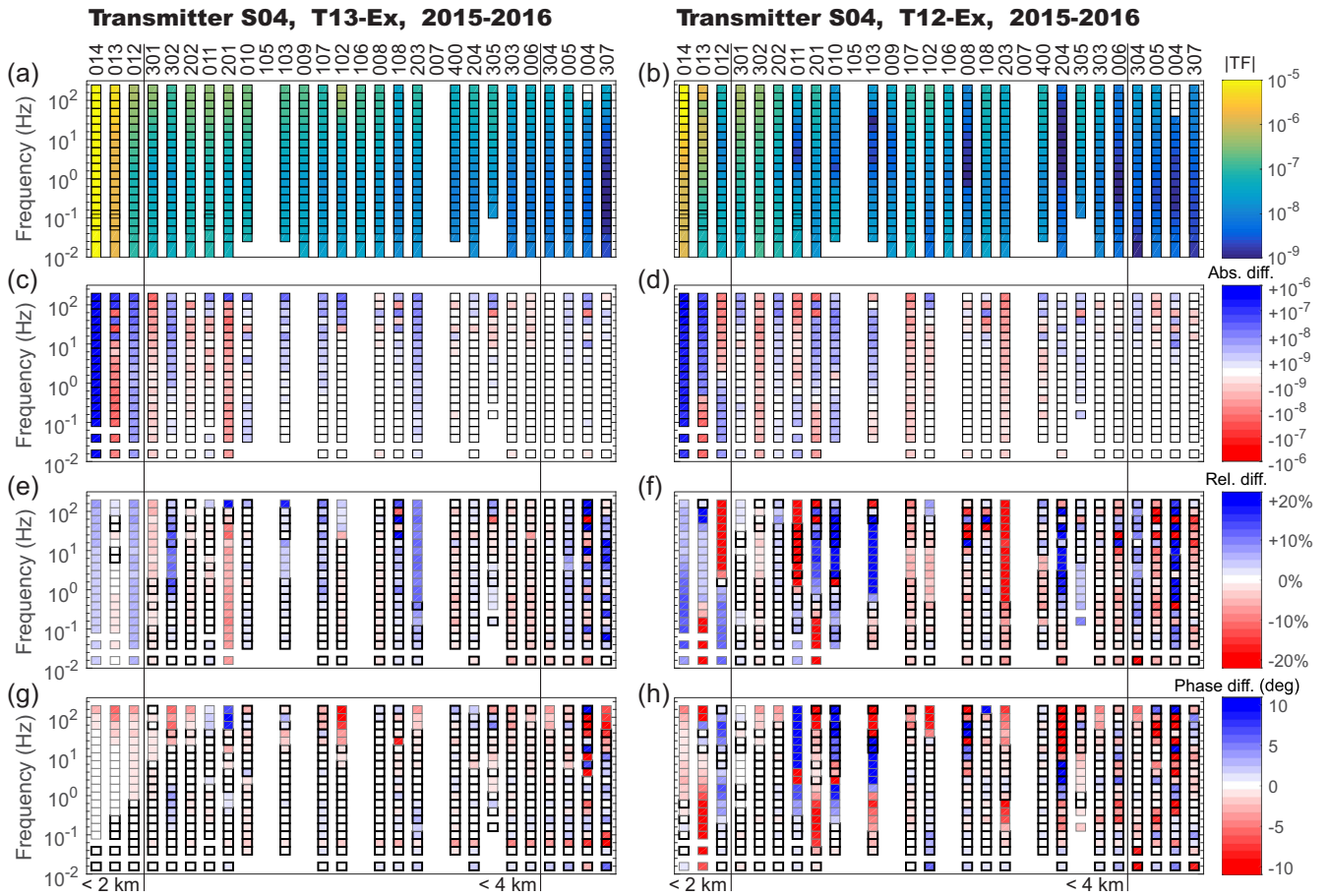
Figure 6. CSEM TFs (a)–(b) and TF changes between subsequent surveys for transmitter S04 and time-lapse period 2015–2016 (c)–(h). Left-hand column: TF T_{13}-E_x; right-hand column: T_{12}-E_x. (a–b) Amplitudes of TFs. (c–d) Absolute and (e–f) relative changes of TF amplitudes, respectively. (g–h) Absolute changes of TF phases. The highlighted markers (thicker outline) in (c)–(h) indicate data points for which time-lapse differences of amplitudes or phases are <3 standard deviations. Vertical lines in (a)–(h) mark source–receiver distances of 2 and 4 km.
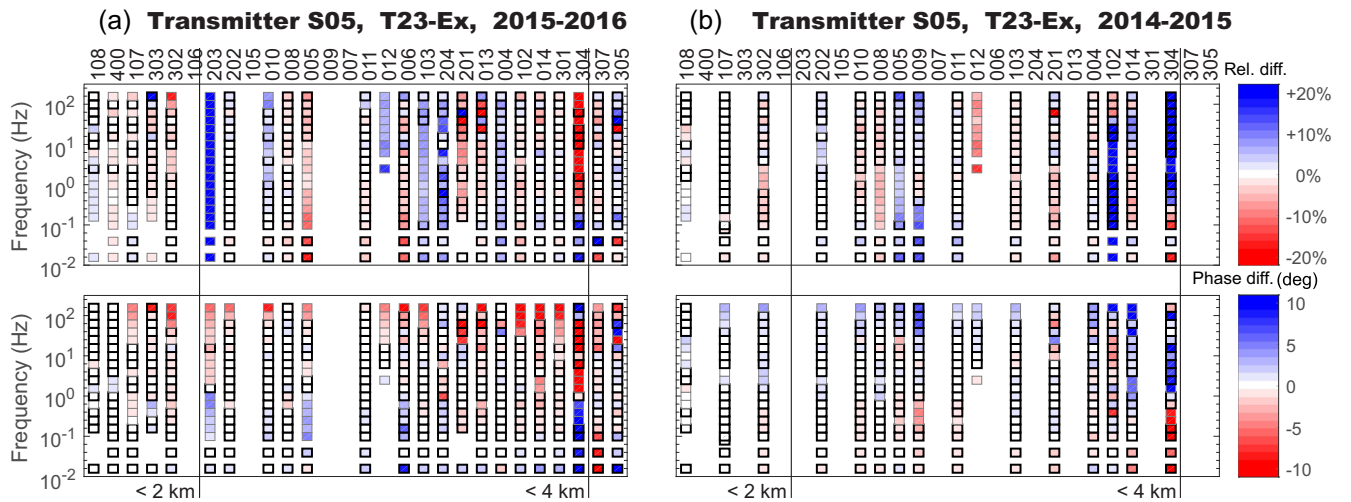

Figure 7. Change of TF T_{23}-E_x of transmitter S05 for time-lapse periods (a) 2015–2016 and (b) 2014–2015. Upper panels in (a) and (b) show relative changes of TF amplitudes; lower panels show absolute changes of TF phases. The bold outlines mark data points for which time-lapse differences are <3 standard deviations. Receivers in (a) and (b) are sorted by radial distance to transmitter S05. Vertical lines mark source–receiver distances of 2 and 4 km.

TF phases show only minimal deviations $<\pm 1°$ over a wide frequency range. Time-lapse differences of amplitudes of the strongest TF component were usually below ± 5 per cent. This also means that the data showing the best repeatability coincide for the Bockstedt oil field with the data of highest sensitivity to the reservoir (*cf.* Tietze *et al.* 2015).

5.3 Measurement of the vertical electric field

Recordings of the vertical electric field were obtained for the 2015 and 2016 surveys for all five transmitters. Additional measurements using only transmitter S01-Bo were made in March 2016 (henceforth referred to as 2016-T; *cf.* Section 4.1) and May 2018. Source–receiver distances measure between 1.5 (S05) and 3.5 km (S04).

For all transmitters, stable TFs could be obtained over the full frequency range (0.0156–200 Hz) and for all six E_z dipoles (see Fig. 2b for receiver configuration). Figs 8(a) and (b) exemplarily show TFs for the longest measured dipole 403 (surface to 188 m depth) and the virtual dipole 423 (140–188 m depth), respectively. In general, smooth behaviour of TF amplitudes and phases over frequency at each E_z receiver illustrates high data quality and physically consistent data for all four field campaigns (Figs 8a and b). For comparison, Fig. 8(c) shows TFs of horizontal fields recorded at the location of the borehole that appear similarly smooth, but amplitudes are 1–2 orders of magnitude higher and range between 10^{-8} and 10^{-6} V A^{-1} m^{-1}. The observations are in good agreement with expectations from modelling studies that suggested that vertical electric fields are typically one or more orders of magnitude smaller than horizontal electric fields (at surface) (e.g. Wirianto *et al.* 2010; Schaller *et al.* 2014; Tietze *et al.* 2015).

For transmitters S01-S and S01-Bo, the observed TFs show very similar amplitude and phase curves for each vertical dipole. However, standard deviations (error bars) of data points associated with S01-Bo are significantly smaller than for S01-S suggesting that the distribution of the source field containing a vertical component (S01-Bo) is superior for measurement of the vertical electric field at the location of the observation borehole.

In order to analyse the noise characteristics of TFs for all five transmitters, the heatmap in Fig. 8(d) illustrates occurrence rates of TF uncertainties versus amplitudes colour-coded for the 2015 (green) and 2016 (blue) main surveys. The diagonal lines in Fig. 8(d) mark relative uncertainties of 100–0.01 per cent of TF amplitudes. Overall, TF amplitudes of E_z vary between 10^{-10} and 10^{-7} V A^{-1} m^{-1} (horizontal extent of cluster in Fig. 8d). Data points with amplitudes around 10^{-7} V A^{-1} m^{-1} can be associated with transmitter S05, which is located at only ~1 km distance to the observation well. For transmitters S01, S02 and S04, located at 2.5–3 km distance TF amplitudes are $<10^{-8}$ V A^{-1} m^{-1}. Standard deviations of amplitudes for TFs of E_z vary between 10^{-11} and 10^{-10} V A^{-1} m^{-1} (vertical extent of cluster) and are about one order of magnitude lower than for horizontal electric fields (*cf.* Figs 4a-c). Hence, despite the low absolute amplitudes of E_z, the relative errors are between 0.1 and 10 per cent (Fig. 8d), that is, in the same range as for horizontal electric fields (*cf.* Figs 4a–c).

As TF amplitudes for E_z stay $<10^{-7}$ V A^{-1} m^{-1} and amplitude errors show similar variation with frequency as horizontal electric fields (*cf.* Fig. 4e), external EM signals are considered the major noise source for the measured vertical electric fields (*cf.* Section 5.1). External EM noise mostly originates from technical installations at or near surface and natural EM variations in the atmosphere.

Within the conductive subsurface, such noise is attenuated and absolute levels of external EM noise are significantly lower for E_z receivers as they reside much deeper in the earth. Hence, we expect that uncertainty estimates for (virtual) borehole-only dipoles are lower than errors of TFs of borehole-to-surface dipoles, but in fact TFs of all six dipoles show similar errors for a particular transmitter. Note, data of borehole-only dipoles were not measured directly but reconstructed from borehole-to-surface measurements (*cf.* Section 3). Hence, also these data may suffer from, for example, surface noise transferred into the earth via the cable. If E_z-data for borehole-only dipoles are measured directly between borehole electrodes and within the borehole, data quality may be even higher.

5.4 Repeatability of the vertical electric field

In contrast to surface receivers and transmitters, the sensor chain for observation of the vertical electric field in the borehole (E1–E3 in Fig. 2a) was left in place since its installation in September 2015. Reference electrodes at surface (E0 in Fig. 2a) were installed permanently at the beginning of the main survey in October 2015. Visual comparison of TF curves obtained in 2015, 2016 and two test surveys (Figs 8a–b) reveals excellent agreement of both amplitude and phase behaviour and suggests that repeatability of E_z measurements and processing is similar as for horizontal electric fields (Fig. 8c).

As outlined in Section 4.2, linear combinations of the TFs obtained from processing can be used to synthesize responses for arbitrary source polarizations. In other words, TFs represent electric fields observed at particular polarization angles of the source, but combinations of TFs allow estimation and visualization of responses within a continuous polarization range. This procedure allows to check consistency of the data and can be used to extract responses at polarizations that provide maximum signal levels or maximum sensitivity to target structures (Streich *et al.* 2013).

Fig. 9(a) demonstrates this (calculated) rotation of source polarization for transmitter S01-Bo for the same borehole (403, 423) and surface (400) receivers as shown in Figs 8(a)–(c) for the 2015 survey. In general, electric field observations for source polarizations of 0–180° and 180–360° only differ in the sign of real and imaginary parts. Hence, amplitudes for both polarization ranges are identical and phases differ by 180° as can be seen for receiver 403 (left-hand column in Fig. 9a). For all other source–receiver combinations in Fig. 9(a), the plot range was, therefore, limited to 0–180°. TF components shown in Figs 8(a)–(c) correspond to source polarizations of 30° (T_{12}), 330° (T_{13}) and 270° (T_{23}). For example, for receiver 403 Fig. 9(a) shows that T_{12}-E_z, corresponding to a source polarization of 30°, is close to a minimum of E_z amplitudes (blue colours between 0 and 20° in upper panel of Fig. 9a). Fig. 8(a) confirms that amplitudes of T_{12} (triangles) are up to one order of magnitude lower than for the other components. Also, phases of T_{12}-E_z vary around $\pm 180°$ crossing the $\pm 180°$ limit twice at ~30 and ~1 Hz (Fig. 8a). In the phase plot of Fig. 9(a), this is expressed as alternating the yellow and blue colours for the polarization of 30°.

Electric fields at receivers 403 and 423 show very similar amplitude and phase behaviour over the full source polarization range, confirming consistency of the borehole measurements. E_z amplitudes are strongest at source polarizations around 90° (and 270°). For the E_x component measured at surface (receiver 400), however, highest amplitudes (yellow colours) occur for source polarizations of 135–180°.
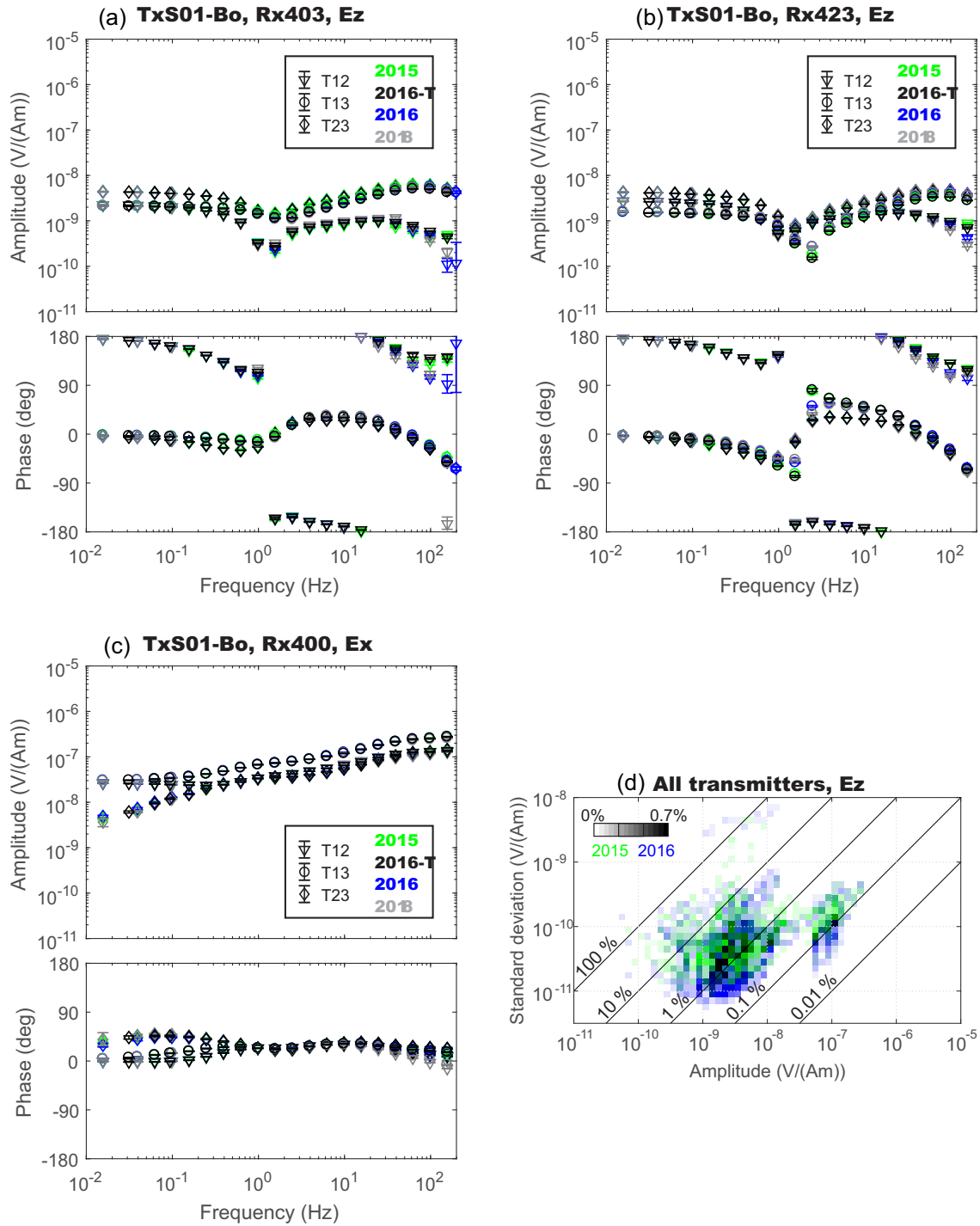
Figure 8. (a–c) Comparison of TFs for transmitter S01-Bo obtained for the vertical electric field within the observation borehole and horizontal components at its surface location for four surveys. (a) Vertical electric field for the longest dipole 403 (*cf.* Fig. 2b for receiver layout), (b) vertical electric field for virtual receiver 423 (140–188 m depth) and (c) horizontal field component E_x at surface (receiver 400). Symbols in (a)–(c) represent TF components and colours mark year of survey (2015–blue; 2016–green, test measurements in spring 2016–black, test measurements in spring 2018–grey). (d) Heatmap of standard deviations of TFs versus TF amplitudes of vertical electric fields colour-coded for the 2015 (green) and 2016 (blue) surveys for all transmitters. Analysis includes TFs T_{12}, T_{13} and T_{23}. Fully saturated pixels correspond to occurrence rates of ≥ 0.7 per cent. The diagonal lines in (a)–(c) mark uncertainty-to-amplitude ratios of 100–0.01 per cent.

We also studied repeatability of the three receivers for the full polarization range. Fig. 9(b) shows relative differences of amplitudes (upper panels) and absolute differences of phases (lower panels) for the data of Fig. 9(a). As before, blue and red colours in time-lapse plots indicate increase and decrease of corresponding field values, respectively. Results for receiver 403 (left-hand column in Fig. 9b) illustrate that polarization ranges of 0–180° and 180–360° convey redundant information as change patterns are repeated.
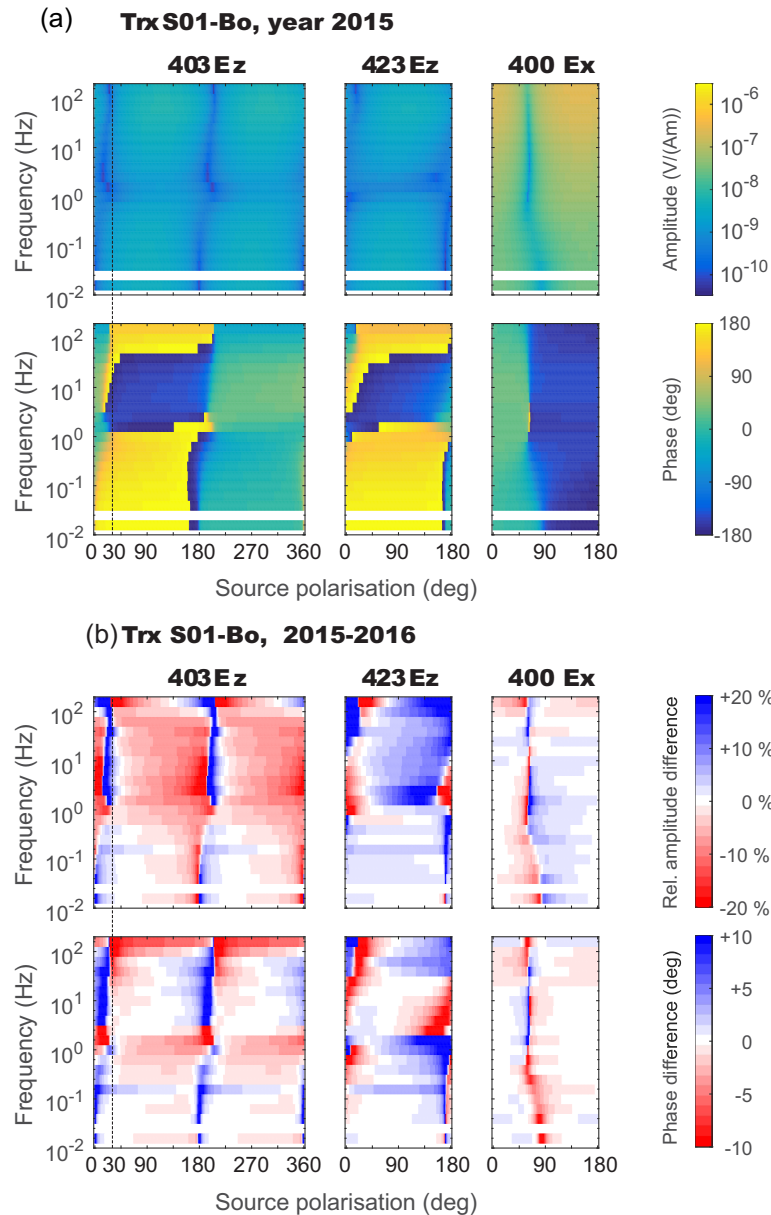
Figure 9. (a) Calculated electric field at receivers 403 (E_z), 423 (E_z) and 400 (E_x) for rotating source polarization of transmitter S01-Bo; upper and lower panels show colour-coded field amplitudes and phases, respectively. (b) Change of electric fields of (a) between 2015 and 2016. Upper and lower panels show relative differences of amplitudes and absolute differences of phases, respectively.

As expected, time-lapse differences between the 2015 and 2016 measurements vary with polarization angles (Fig. 9b). Largest deviations (blue and red colours) are usually found at source polarizations where amplitudes are smallest (0/180° for E_z, 90° for E_x) and signal-to-noise ratios are poor. In return, where fields are strongest (60–120° for E_z, 135–180° for E_x), lowest deviations between the 2015 and 2016 measurements are observed as indicated by less intense colouring.

At these 'optimal' polarizations of 60–120°, E_z phases of transmitter S01-Bo at dipole 403 (first column of Fig. 9b) usually agree within ±2° (white colours in bottom panel of Fig. 9b), except for the highest frequencies >50 Hz and frequencies around 1 Hz (red colours) where field amplitudes are minimal (*cf.* blue colours in

top panel of Fig. 9a). Corresponding amplitudes show excellent repeatability within ≤±3 per cent at frequencies <1 Hz. At higher frequencies, data at dipole 403 show a uniform increase of amplitudes of +5 to +10 per cent for frequencies (red colours in top panel). For the borehole-only E_z dipole 423 (second column in Fig. 9b), amplitude and phase differences are of similar size as for receiver 403, but have opposite sign (the blue and red colours interchanged).

Horizontal fields of transmitter S01-Bo measured at surface receiver 400 (third column in Fig. 9b) show overall smaller differences between 2015 and 2016 than vertical electric fields, in particular at frequencies >1 Hz. At the maximum polarization of E_x (∼0/180°), time-lapse changes are <±2 per cent for amplitudes and <±1° for phases over the entire frequency range. Amplitudes of horizontal

electric fields are up to two orders of magnitudes larger than vertical electric fields at frequencies >1 Hz. Relative differences of E_z measurements at these frequencies are larger (5–10 per cent) than for E_x (∼1 per cent) but absolute variations of field amplitudes are lower for E_z than for E_x.

The results in Fig. 9(b) can also be used to estimate the 'optimal' polarization angle for transmitter S01-Bo at which agreement between the 2015 and 2016 measurements is highest. As measure of agreement, we calculated the (non-normalized) rms misfit between observations of 2015 and 2016, that is, the sum of squared differences of field amplitudes (or phases) over the entire frequency range (Figs 10a and b). For all six receivers (coloured lines in Fig. 10), misfit versus polarization angle curves for both amplitudes and phases show a distinct maximum (poor agreement) at an angle of about 20°. Best agreement (lowest misfits) of amplitudes is found between 45° and 90°. For phases, borehole-only receivers (412–423) show a clear minimum at about 66° (Fig. 10a), whereas results for the three dipoles reaching to surface (401–403) exhibit less pronounced and very broad minima between 45° and 160°. Based on these results and considering that phases usually showed higher repeatability than amplitudes, an angle of 66° was chosen as 'optimal' source polarization for transmitter S01-Bo and all six E_z dipoles. Similarly, optimal polarizations were determined for the other four transmitters.

Figs 11(a)–(e) provide an overview of the time-lapse differences of all six E_z dipoles for each of the five transmitters at the optimal polarization angle. Most obviously and as already observed for horizontal electric fields, repeatability decreases with increasing source–receiver distance. For transmitter S05 located closest to the borehole at 1.5 km distance, amplitudes and phases could be repeated within ±1 per cent (except for dipole 401) and ±1°, respectively, over the full frequency range. Largest variability between measurements occurs for the most distant transmitter S04 (3.5 km) with differences exceeding ±20 per cent and ±10° at dipoles reaching surface (401–403).

More importantly, differences at borehole-only dipoles (412–423) are significantly lower than for measurements of electric dipoles reaching surface (401–403) for all transmitter locations. At receivers 412–423, differences commonly measure <5 per cent and <2° over the entire frequency range and appear nearly independent of data quality at receivers 401–403. These observations suggest that noise collected in the upper 92 m of the sensor system cancels out for dipoles 412–423.

Repeatability also improves with increasing dipole lengths as amplitudes of measured fields rise and signal-to-noise ratios improve. Considering dipoles 401–403, amplitude and phase differences are largest for the 92 m dipole (401) and smallest for the 188 m long receiver (403) for all transmitters. Similarly, for each transmitter differences for dipole 413 (92 m) are smaller than for dipoles 412 and 423 (48 m).

Figs 11(f)–(j) analyse variations of E_z for S01-Bo in more detail between subsequent installations of the transmitter in main and test surveys (*cf.* Section 4.1). The apparently large differences occurring between measurements taken in September and October 2015 (dark blue colours Fig. 11f) at receivers 401–403 result from reconfiguration of the surface electrodes at the beginning of the main survey in October 2015 (*cf.* Section 3) and can be considered self-induced. E_z data of the (virtual) dipoles are expected to be independent of the exact receiver layout at surface and TF amplitudes processed for receivers 412–423 show virtually no changes during this time. Corresponding phases are similarly stable at frequencies <1 Hz but show a decrease of more than 10° for frequencies >10 Hz, which may be

associated with changes in near-surface resistivities at the transmitter (*cf.* Fig. 7). For the following time-lapse periods (Figs 11g–j), the E_z receiver configuration was not changed and variations of both amplitudes and phases are significantly smaller for all six dipoles. In particular, size of changes seems to decrease with time, being smallest between October 2016 and May 2018 (Fig. 11j). Based on the results in Figs 11(f)–(j), we speculate that integrity and quality of E_z receivers remained constant over time and electrochemical conditions within the observation borehole assumed a stable state.

In short, although vertical electric fields at shallow depth have significantly smaller amplitudes than horizontal components, they show excellent repeatability with phase and amplitude differences usually <±2° and <±5 per cent for borehole-only dipoles, which is in a similar range as for (the much larger) horizontal electric fields. For dipoles reaching surface, variability between measurements is often higher as signal-to-noise ratios are poorer. Repeatability values of <±2° and <±5 per cent were achieved for transmitters located close to the source (S05) or containing a vertical component (S01-Bo).

6 DISCUSSION AND CONCLUSIONS

We investigated the repeatability of land-based CSEM measurements in an active oil field in practice including for the first time measurements of the vertical electric field with a newly developed modular receiver chain installed in a 200 m deep observation well. Equipped with three electrodes, vertical dipoles reaching from surface to depths of 92, 140 and 188 m, respectively, were established. Observed amplitudes of CSEM signals in E_z are one to two orders of magnitude smaller than horizontal field components measured at surface that agrees with results from existing modelling studies (Wirianto *et al.* 2010; Schaller *et al.* 2014; Tietze *et al.* 2015). Processing of E_z recordings resulted in TFs that are stable and coherent over the entire frequency range (200–0.0156 Hz) indicating high quality and physical consistency of the E_z recordings.

The overall quality of individual measurements for all electric field components was constant over a time span of 2.5 yr. For both horizontal and vertical electric fields standard deviations of TF estimates vary between 0.1 and 10 per cent of TF amplitudes, centring at around 1 per cent for all CSEM surveys. Error levels above 10 per cent were limited to few receivers and could be attributed to strong disturbances by nearby cultural noise sources. We would like to emphasize that despite the inherently low CSEM signal amplitudes of E_z, relative errors of TFs for E_z are in the same range as for horizontal electric fields. These results indicate that noise conditions at depth are more favourable than at surface but also that the new E_z receiver produced stable results over a time span of more than 2.5 yr.

Closer inspection of measurements revealed that data uncertainties change their character depending on the signal-to-noise ratio at the receiver position. For TFs observed in the vicinity of the source (<2 km distance), that is, where TF amplitudes are highest (>10^{-7} V A^{-1} m^{-1}), uncertainties are proportional to TF amplitudes measuring ∼0.1–0.3 per cent as they are dominated by intrinsic noise of the measuring system. For TFs with amplitudes <10^{-7} V A^{-1} m^{-1}, corresponding to source–receiver distances >2 km in Bockstedt, external EM noise resulting from natural EM field variations (MT signal) and technical installations becomes significant and dominates for receivers located >4 km from the transmitter. At distances >4 km, standard deviations of TFs assume minimum absolute values of 10^{-9}–10^{-10} V A^{-1} m^{-1} with
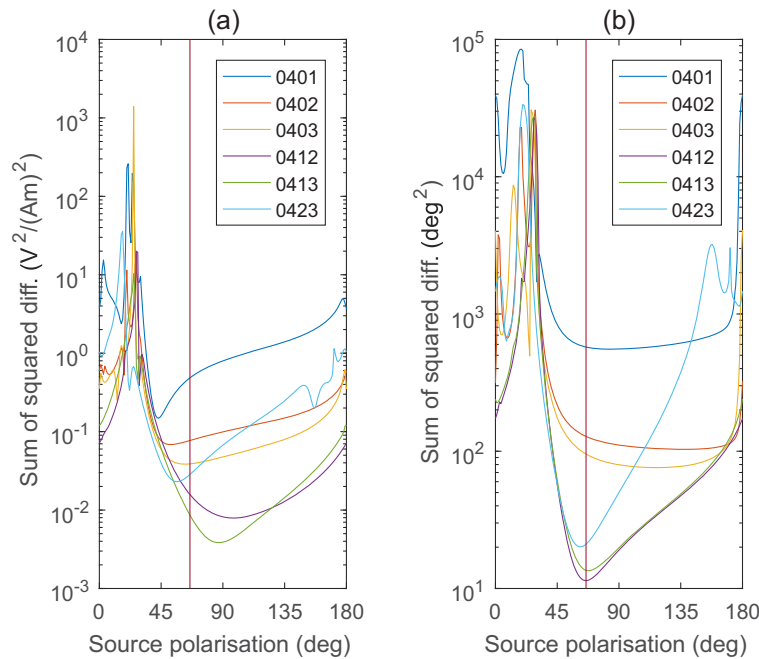
Figure 10. RMS error between electric fields of the 2015 and 2016 measurements (transmitter S01-Bo) summed up over all frequencies for each of the six E_z receivers (line colours) and source polarization angles of 0–180°. (a) Amplitudes and (b) phases. Vertical lines in (a) and (b) mark 'optimal' polarization angles (see text).

lowest values at frequencies of 0.1–10 Hz. Overall, highest data quality (lowest relative data errors) is observed for source–receiver distances of 2–4 km and frequencies <10 Hz and results for the 2015 and 2016 measurements agree with analyses of the 2014 data set by Tietze *et al.* (2015).

Repeatability of electric field measurements between surveys is mainly controlled by the signal-to-noise conditions and is generally highest for data with highest quality (lowest uncertainties) in individual surveys. For horizontal components, best agreement between consecutive measurements was observed for source–receiver distances between 2 and 4 km and frequencies <10 Hz. For these data, TF phases and amplitudes usually agree within ± 1° and ± 5 per cent, respectively. Phases and amplitudes of the vertical electric field usually also agree within ± 2° and ± 5 per cent, respectively. In particular, data obtained with 'borehole-only' dipoles located between 92 and 188 m depth show phase differences <±1° over a wide frequency range.

For about 50 per cent of all data points significant time-lapse differences exceeding 3 standard deviations were observed. Such differences are often associated with particularly low TF amplitudes, for example, the weakest of the three polarizations. Yet, the analyses also outlined two additional conditions that can significantly impair repeatability: (i) relocation errors and (ii) near-surface resistivity changes.

Measured and simulated time-lapse responses suggest that errors in sensor relocation of a few tens of metres between surveys can result in TF differences >±20 per cent and >±5°, respectively. The degree of impairment is correlated with the gradient of the electric field at the receiver position, that is, depends on the transmitter geometry and the underlying conductivity structure. While location differences can be considered in modelling and/or inversion of time-lapse data, direct comparison of TFs is not possible in such situations but can lead to erroneous interpretations with respect to

4-D resistivity structures. Precise position measurements, for example, using differential GPS, are recommended to (re-)locate survey equipment and minimize relocation errors. Ideally, receivers and sources can be installed permanently.

At least for our data sets, variability of TFs between surveys is significantly higher at frequencies >10 Hz than at lower frequencies. Amplitudes of these changes differ both between transmitters and between time intervals, yet appear to be consistent for each time-lapse period. We speculate that weather conditions or other seasonal influences could result in modifications of soil properties such as temperature or humidity and potentially cause the observed changes in TFs. For transmitter S05, for example, TF phases change by 2–8° for the interval 2015–2016 in this frequency range. 1-D simulations confirm that such amplitude changes can be explained if resistivity increases by a factor of 2 in the upper 10 m, while the TF amplitudes remain nearly unaffected at the same time.

While permanent installation of instruments would help avoiding redeployment errors, influence of seasonal changes of soil properties would persist. Impact of near-surface changes may be reduced, though, if sensors are placed at greater depth.

As far as we know, very few other publications exist on the repeatability of CSEM measurements. For a first repeat test during the 2014 survey, Tietze *et al.* (2015) reported TF differences as low as <1 per cent with recordings 10 d apart, while part of their equipment was left in place between the two measurements. Vilamajó *et al.* (2015) estimated repeatability errors of ±10 per cent and ±5° for horizontal electric fields and CSEM transmissions, respectively, at two subsequent days at the Hontomín CO$_2$ storage site. Yet the authors describe a significant drift of electric field measurements, which were carried out using bare steel electrodes, that probably impaired the measurements.

Repeatability levels also play an important role for the interpretation of (numerical) studies on the applicability of CSEM methods for monitoring. To be detectable, time-lapse differences resulting
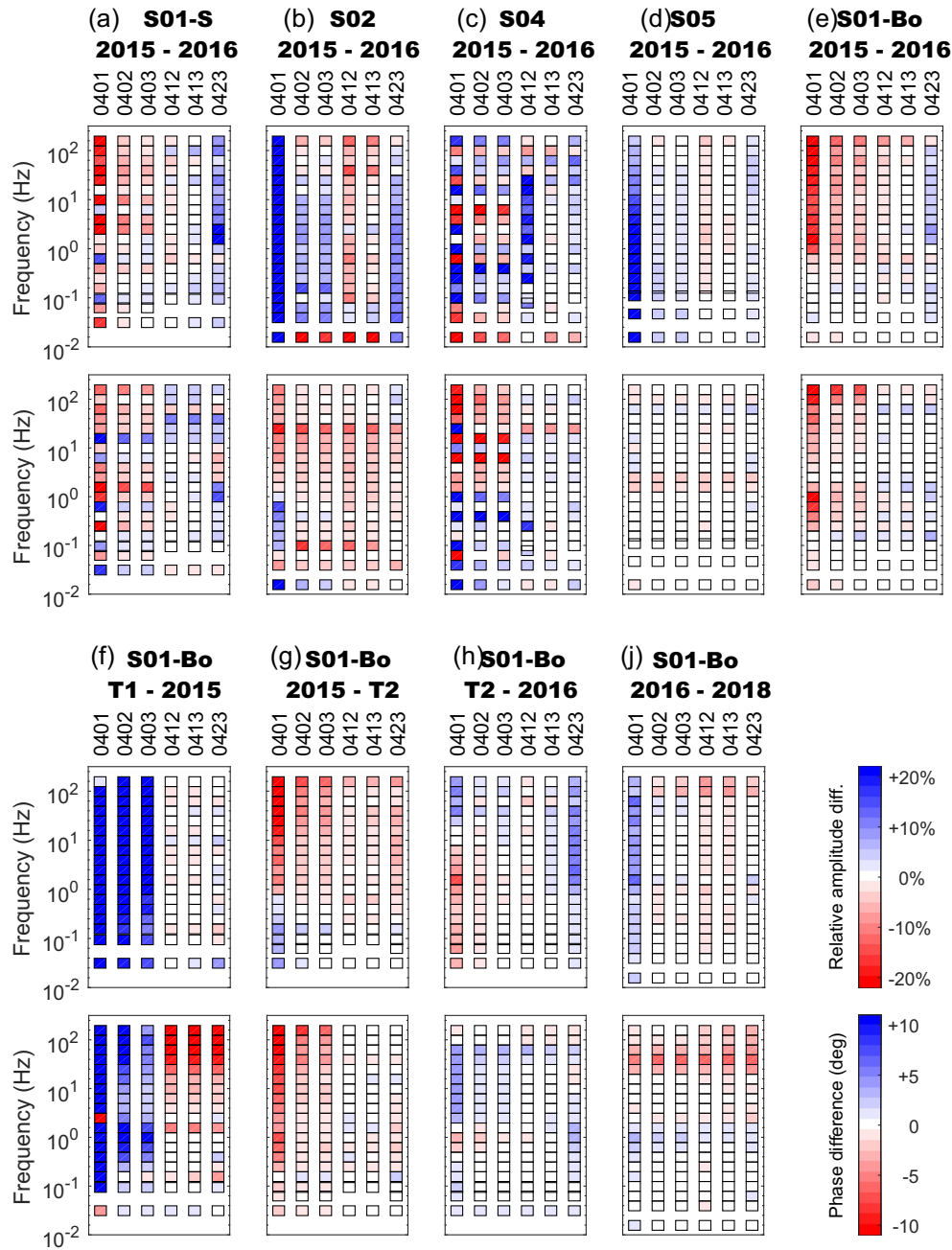
Figure 11. Change of E_z for various transmitters between selected surveys using the optimal source polarization angle α (see text). (a–e) Change between the 2015 and 2016 main surveys for transmitters (a) S01-S (surface variant), $\alpha = 110°$, (b) S02, $\alpha = 85°$, (c) S04, $\alpha = 150°$, (d) S05, $\alpha = 95°$ and (e) S01-Bo, $\alpha = 66°$. (f–i) Change for transmitter S01-Bo between (f) September–October 2015, (g) October 2015–March 2016, (h) March–October 2016 and (j) October 2016–May 2018.

from conductivity changes in the target formation have to exceed the uncertainty threshold for repeat measurements significantly. In most studies, a repeatability error as low as 1 per cent is considered achievable (e.g. Wirianto *et al.* 2010; Schamper *et al.* 2011; Vilamajó *et al.* 2013; Tietze *et al.* 2015). In view of the results obtained in Bockstedt, however, we consider such low repeatability errors rather optimistic.

Based on the outcome of the Bockstedt time-lapse experiment, we expect that overall repeatability errors of $\leq\pm5$ per cent and $\leq\pm1°$ can be achieved in practice even in high noise areas, but only if surveying schemes are tuned accordingly. Data

quality of single measurements provides a good proxy for a first estimate of repeatability. Essential surveying procedures are (i) permanent installation of sensors or minimizing relocation errors, (ii) deploying high-quality sensors such as electrochemically buffered electrodes, (iii) application of robust data processing routines and (iv) optimizing source currents. In other cases, more conservative estimates of repeatability errors in the order of 5 or even 10 per cent may be more appropriate. Such values may appear large in view of time-lapse signals of resistivity changes in target formations that are often expected in a similar range of values.

REFERENCES

Alumbaugh, D.L. & Morrison, H.F., 1995. Theoretical and practical considerations for crosswell electromagnetic tomography assuming a cylindrical geometry, *Geophysics,* **60,** 846–870.

Araya, J. & Ritter, O., 2016. Source effects in mid-latitude geomagnetic transfer functions, *Geophys. J. Int.,* **204**(1), 606–630.

Bahr, K., 1983. Joint interpretation of magnetotelluric and geomagnetic data and local telluric distortions, *J. Geomagn. Geoelectr.,* **35**(11–12), 555–566.

Betz, D., Führer, F., Greiner, G. & Plein, E., 1987. Evolution of the Lower Saxony Basin, *Tectonophysics,* **137,** 127–170.

Bindoff, N.L., Filloux, J.H., Mulhearn, P.J., Lilley, F.E.M. & Ferguson, I.J., 1986. Vertical electric field fluctuations at the floor of the Tasman Abyssal Plain, *Deep-Sea Res.,* **33**(5), 587–600.

Börner, J.H., Bär, M. & Spitzer, K., 2015a. Electromagnetic methods for exploration and monitoring of enhanced geothermal systems: a virtual experiment, *Geothermics,* **55,** 78–87.

Börner, J.H., Wang, F., Weißflog, J., Bär, M, Görz, I. & Spitzer, K., 2015b. Multimethod virtual electromagnetic experiments for developing suitable monitoring designs: a fictitious CO_2 sequestration scenario in Northern Germany, *Geophys. Prospect.,* **63**(6), 1430–1449.

Cagniard, L., 1953. Basic theory of the magneto-telluric method of geophysical prospecting, *Geophysics,* **18**(3), 605–635.

Chave, A.D. & Filloux, J.H., 1985. Observation and interpretation of the seafloor vertical electric field in the eastern North Pacific, *Geophys. Res. Lett.,* **12,** 793–796.

Colombo, D. & McNeice, G., 2017. Geophysical monitoring of waterflooding in Saudi Arabia: methods and perspectives, in *SEG Technical Program Expanded Abstracts 2017,* pp. 1044–1048.

Constable, S., 2010. Ten years of marine CSEM for hydrocarbon exploration, *Geophysics,* **75**(5), 67–81.

Forbush, S.E., 1933. Apparent vertical earth-current variations at the Huancayo magnetic observatory, *Terr. Magn. Atmos. Electr.,* **38,** 1–12.

Girard, J.-F., Coppo, N., Rohmer, J., Bourgeois, B., Naudet, V. & Schmidt-Hattenberger, C., 2011. Time-lapse CSEM monitoring of the Ketzin (Germany) CO_2 injection using 2xMAM configuration, *Energy Procedia,* **4,** 3322–3329.

Guéguen, Y. & Palciauskas, V., 1994. *Introduction to the Physics of Rocks,* Princeton University Press.

Håland, E., Flekkøy, E.G. & Måløy, K.J., 2012. Vertical and horizontal components of the electric background field at the sea bottom, *Geophysics,* **77**(1), E1–E8.

Holten, T. & Flekkøy, E.G., 2011. Time lapse CSEM measurements for reservoir monitoring using a vertical receiver-transmitter setup, in *SEG Annual Meeting 2011 San Antonio, Expanded Abstract,* pp. 697–701.

Holten, T., Flekkøy, E.G., Singer, B.Sh., Blixt, E.M., Hanssen, A. & Måløy, K.J., 2009. Vertical source, vertical receiver, electromagnetic technique for offshore hydrocarbon exploration, *First Break,* **27,** 89–93.

Jones, F.W. & Geldart, L.P., 1967a. Vertical telluric currents, *Earth planet. Sci. Lett.,* **2,** 69–74.

Jones, F.W. & Geldart, L.P., 1967b. Vertical telluric currents at separated locations, *Earth planet. Sci. Lett.,* **2,** 174–176.

Kockel, F., Wehner, H. & Gerling, P., 1994. Petroleum systems of the Lower Saxony Basin, Germany, eds ,Magoon, L.B. & ,Dow, W.G., in *The Petroleum System—from Source to Trap,* American Association of Petroleum Geologists, pp. 573–586.

Leonhardt, B., Visser, F., Lessner, E., Wenzke, B. & Schmidt, J., 2011. From flask to field—the long road to development of a new polymer, in *Expanded abstract, 16th European Symposium on Improved Oil Recovery,* Cambridge, UK, 12–14 April, B05, pp. 14, doi: 10.3997/2214-4609.201404775.

Myer, D., Constable, S., Key, K., Glinsky, M.E. & Liu, G., 2012. Marine CSEM of the Scarborough gas field, Part 1: experimental design and data uncertainty, *Geophysics,* **77**(4), E281–E299.

Ritter, O. *et al.*, 2015. A permanent magnetotelluric reference station in Wittstock, Germany, Potsdam: Deutsches GeoForschungsZentrum GFZ, Tech. Rep., pp. 10, doi:10.2312/GFZ.b103-15092.

Schaller, A., Hunziker, J., Streich, R. & Drijkoningen, G., 2014. Sensitivity of the near-surface vertical electric field in land controlled-source electromagnetic monitoring, in *SEG Denver 2014 Annual Meeting Expanded abstract,* pp. 838–843.

Schamper, C., Rejiba, F., Tabbagh, A. & Spitz, S., 2011. Theoretical analysis of long offset time-lapse frequency domain controlled source electromagnetic signals using the method of moments: application to the monitoring of a land oil reservoir, *J. geophys. Res.,* **116,** B03101, doi:10.1029/2009JB007114.

Strack, K., 2014. Future directions of electromagnetic methods for hydrocarbon applications, *Surv. Geophys.,* **35**(1), 157–177.

Streich, R., 2016. Controlled-source electromagnetic approaches for hydrocarbon exploration and monitoring on land, *Surv. Geophys.,* **37,** 47–80.

Streich, R., Becken, M. & Ritter, O., 2010. Imaging of CO_2 storage sites, geothermal reservoirs, and gas shales using controlled-source magnetotellurics: modeling studies, *Geochemistry,* **70**(S3), 63–75.

Streich, R., Becken, M., Matzander, U. & Ritter, O., 2011. Strategies for landbased controlled-source electromagnetic surveying in high-noise regions, *Leading Edge,* **30**(10), 1174–1181.

Streich, R., Becken, M. & Ritter, O., 2013. Robust processing of noisy land-based controlled-source electromagnetic data, *Geophysics,* **78**(5), E237–E247.

Tietze, K, Ritter, O. & Veeken, P., 2015. Controlled-source electromagnetic monitoring of reservoir oil-saturation using a novel borehole-to-surface configuration, *Geophys. Prospect.,* **63**(6), 1468–1490.

Tietze, K., Ritter, O., Patzer, C. & Veeken, P., 2018. Borehole controlled-source electromagnetics for hydrocarbon-saturation monitoring in the Bockstedt oil field, Onshore Northwest Germany, *SPE Reservoir Eval. Eng.,* **21,** doi:10.2118/183165-PA.

Vilamajó, E., Queralt, P., Ledo, J. & Marcuello, A., 2013. Feasibility of monitoring the Hontomín (Burgos, Spain) CO_2 storage site using a deep EM source, *Surv. Geophys.,* **34,** 441–461.

Vilamajó, E., Rondeleux, E., Queralt, P., Marcuello, A. & Ledo, J., 2015. A land controlled-source electromagnetic experiment using a deep vertical electric dipole: experimental settings, processing, and first data interpretation, *Geophys. Prospect.,* **63,** 1527–1540.

Wilt, M.J., Alumbaugh, D.L., Morrison, H.F., Becker, A., Lee, K.H. & Deszcz-Pan, M., 1995. Crosswell electromagnetic tomography: system design considerations and field results, *Geophysics,* **60**(3), 871–885.

Wirianto, M., Mulder, W.A. & Slob, E.C. 2010. A feasibility study of land CSEM reservoir monitoring in a complex 3-D model, *Geophys. J. Int.,* **181,** 741–755.

Zach, J.J., Frenkel, M.A., Ridyard, D., Hincapie, J., Dubois, B. & Morten, J.P., 2009. Marine CSEM time-lapse repeatability for hydrocarbon field monitoring, in *SEG International Meeting and Exhibition Houston Expanded Abstract,* pp. 820–824.

Zhdanov, M.S., Endo, M., Black, N., Spangler, L., Fairweather, S., Gibbs, A., Eiskamp, G.A. & Will, R., 2013. Electromagnetic monitoring of CO_2 sequestration in deep reservoirs, *First Break,* **31,** 85–92.

Ziegler, P.A., 1987. Late cretaceous and cenozoic intra-plate compressional deformations in the Alpine foreland—a geodynamic model, *Tectonophysics,* **137,** 389–420.

Ziolkowski, A., Parr, R., Wright, D., Nockles, V., Limond, C., Morris, E. & Linfoot, J., 2010. Multitransient electromagnetic repeatability experiment over the North Sea Harding field, *Geophys. Prospect.,* **58,** 1159–1176.

SUPPORTING INFORMATION

Supplementary data are available at *GJI* online.

Figure S1. Spatial distribution of CSEM fields. (a) 1-D layered half-space model reflecting the average resistivity distribution in the Bockstedt survey area (Tietze *et al.* 2015). (b and c) Map view of TF T_{13}-E_x simulated for transmitter S01-Bo at a frequency of 0.0986 Hz using the layered half-space model of (a). Colours and isolines show (b) log10 amplitudes of TFs and (c) TF phases. Red lines indicate location of active wires of transmitter S01-Bo. Circles mark locations of 26 receivers deployed during the 2014 main survey. Filled circles with labels mark stations that were moved by more than 40 m between the 2014 and 2015 main surveys. Circles with fillings and labels in red indicate that both amplitudes and phases changed; circles with fillings and labels in black indicate a change in amplitude only (*cf.* Fig. S2).

Figure S2. Influence of receiver position on CSEM TFs. (a and b) Simulated differences of CSEM TF T_{13}-E_x of transmitter S01-Bo between receiver locations of the 2014 and 2015 field surveys. Responses for both survey configurations were generated using the 1-D model of Fig. S1(a). Colours show (a) relative differences of TF amplitude versus frequency, and (b) absolute differences of TF phase versus frequency. The white colours indicate amplitude and phase changes $\leq\pm1$ per cent and $\leq\pm0.5°$, respectively; the blue (red) colours mark increase (decrease) of values from 2014 to 2015. (c and d) Observed differences between measurements of T_{13}-E_x of transmitter S01-Bo obtained in the 2014 and 2015 field surveys, displayed as (c) relative differences of TF amplitude and (d) absolute differences of TF phase. Receivers are sorted by radial distance to the centre of mass of transmitter S01-Bo. Red labels mark receivers moved by more than 40 m between surveys. Bold framed pixels in (c) and (d) mark differences that lie within 3 standard deviations (see Section 5.2). Vertical lines in (a) and (b) mark source–receiver distance of 2 km.

Please note: Oxford University Press is not responsible for the content or functionality of any supporting materials supplied by the authors. Any queries (other than missing material) should be directed to the corresponding author for the paper.